Proc. Vth International Workshop, Advances in Signal Processing for Non Destructive Evaluation of Materials
Québec City (Canada),2-4 Aug. 2005. © X. Maldague ed., É. du CAO (2006), ISBN 2-9809199-0-X

**Invited paper**

# Pulsed thermography: philosophy, qualitative & quantitative analysis on aircraft materials & applications

N.P. Avdelidis*[1], D.P. Almond[2], Z.P. Marioli-Riga[1], A. Dobbinson[2], B.C. Hawtin[3]

*[1] Hellenic Aerospace Industry, Department of Research and Product Design, PO Box 23, 32009 Schimatari, Greece; [2] Materials Research Centre, University of Bath, Bath BA2 7AY, United Kingdom; [3] Airbus UK, Filton, Bristol BS99 7AR, United Kingdom.*

## Abstract

Thermal non-destructive testing (NDT) is commonly used for assessing aircraft structures. This research work evaluates the potential of pulsed thermography (PT) for certain applications. In particular, real time monitoring was obtained using PT. In some cases, thermal modelling as well as other non-destructive testing and evaluation techniques (i.e. acoustography, ultrasonic wheel array) were also used with the intention of providing supplementary results. The following features were studied and presented:

- Through skin sensing on aluminium (Al) alloy and carbon fibre reinforced plastic (CFRP) structures.
- Defect detection under multi-ply composite repairs.
- Impact damage on carbon fibre reinforced plastic panels and honeycomb sandwich structures.
- Drilling induced defects on multi-ply laminates of carbon fibre composites.

It is concluded that PT is a rapid large area non-destructive technique that can find adequate use on aircraft – aerospace materials and structures.

**Keywords:** pulsed thermography, NDT, aircraft, defect detection, quantitative assessment, through skin sensing.

## 1. Theoretical Background on Thermal NDT

Infrared - thermal investigation techniques have been used successfully in several of applications, i.e. inspection of subsurface defects and features, identification of thermo-physical properties, detection of coating thickness and hidden structures [1]. There are two approaches that can be used: passive [2] and active [3]. The passive approach is commonly used in the investigation of materials that are at different temperature (regularly higher) than ambient, whilst in the case of the active approach a thermal excitation source is employed with the intention of inducing thermal contrasts [4].

In the active approach of the thermal NDT, pulsed thermography (PT) is a widely used approach for investigating aircraft materials and structures. PT is a popular thermal stimulation technique where the surface under investigation is pulse heated (time period of heating varying from a few milliseconds for high conductive materials such as metals to a few seconds for low conductive materials such as composites) using one or more pulse heating sources and the resulting thermal transient at the surface is monitored using a thermal camera [5].

In the 1980's, Vavilov and Taylor [6] discussed the principles of thermal NDT expressing the ability to provide quantitative information about hidden defects or features in a material. Although thermal NDT

---

* Correspondence: Email: avdel@mail.ntua.gr ; Telephone: +30 - 22620 - 52396 ; Fax: +30 - 22620 - 52290

has the potential to deliver first class results, there are various properties of the material(s) that need to be considered:

- Thermal Properties: conductivity, diffusivity, effusivity, specific heat.
- Spectral Properties: emissivity, absorption, reflection, transmission.
- Other Properties - Characteristics: density, porosity.

All of the above mentioned features are very important when dealing with thermal NDT surveys. For example, when a material presents voids or pores in its structure [7], then its thermal conductivity and density decreases, its thermal diffusivity is altered and so the conduction of heat transfer within the material is affected [8]. This can be realised from the following equation:

$$a = \frac{k}{\rho C_p} \tag{1}$$

where:
$\alpha$ is the thermal diffusivity ($m^2s^{-1}$), k is the thermal conductivity ($Wm^{-1}K^{-1}$), $\rho$ is the density ($kgm^{-3}$) and Cp is the specific heat capacity ($Jkg^{-1}K^{-1}$).

Another consideration when a thermal NDT survey is to be completed is the thermal effusivity of the materials to be tested. Materials with low effusivity values will present higher temperatures, since:

$$T = \frac{Q}{e\sqrt{\pi t}} \tag{2}$$

where:
Q is the input energy (Joules) and e is the thermal effusivity ($Ws^{1/2}m^{-2}K^{-1}$), which can be calculated by:

$$e = \sqrt{k\rho C_p} \tag{3}$$

where:
k is the thermal conductivity ($Wm^{-1}K^{-1}$), $\rho$ is the density ($kgm^{-3}$) and Cp is the specific heat capacity ($Jkg^{-1}K^{-1}$).

Following the early work of Vavilov and Taylor, thermal NDT has been implemented by several groups worldwide [7-11]. Thus, the potential of the technique for detecting and imaging subsurface defects have been greatly enhanced and the defect imaging process is now well understood [12].

## 2. Through skin sensing

The objective of this work was to study the ability of PT for locating anchoring points beneath the outer skin of aircraft structures, to facilitate automated drilling and fixing. Typical test structures, comprising of either Al or CFRP aircraft skin positioned over a thick Al and/or CFRP strut fixture, were investigated experimentally and analysed using finite difference thermal modelling software, taking into consideration the size and depth of the features, as well as their thermal properties [13].

The representative test structures, comprising an Al aircraft skin (1.6mm) positioned over a thick Al strut and of CFRP skin (2mm or 4mm) over a thick CFRP strut, were analysed using the ThermoCalc-3D software. The dimensions of all investigated panels were 500 x 500 mm. The width of the strut was 100 mm. The size and depth of the features, as well as the thermal properties of the investigated materials were taken into account. Furthermore, the effect of thermal contact resistance (the air gap between skin and strut) was also considered. For this reason, the models were run using different values of air gap such as 1, 10, 50 and 100 μm, as well as with having the perfect contact between the two surfaces (zero air gap).

The following remarks can be made from the modelling results:
- The peak contrast of 4mm CFRP skin over CFRP strut is 2 times smaller than that of 2mm CFRP skin over CFRP strut, whilst its time scale (thermal transient phase) is 4 times longer.
- The 4mm CFRP skin over the CFRP strut presents the lowest thermal contrast amongst the tested modelled structures, while its time scale (thermal transient phase) is the longest (i.e. 20 seconds).
- The peak contrast value of Al is approximately 4.65 times greater than that of the CFRP (2mm skin), for zero air gap, since the differences of the Peak ΔT values are 0.05028 K for the Al and 0.0108 K for the CFRP.

For the experimental work, an integrated pulsed thermographic system (Thermoscope) employing a medium wave infrared camera (Merlin 3-5 μm by Indigo) was utilised. The non-destructive evaluation system has an integrated flash heating system with a power output of 2KJ in 2 to 5 ms. The infrared camera uses a cooled indium antimonide detector with a frame rate of 60 Hz and a focal plane array pixel format of 320 (H) x 256 (V). The same panels, similar to thermal modelling, were investigated. The contrast of the thermal images of the subsurface fixtures in relation to time was measured (plots of contrast –vs.- time). Information concerning the centre line of the struts was obtained from the thermal images (a line was marked on the skin surface to show the centre line of the strut).

In the Al case, since the thermal conductivity is exceptionally high, the maximum frame rate (59.88 frames per second) was used for the recording of the images. In order to avoid the high reflectance of Al during investigation and to record thermal images, the sample was painted with a water based black paint. Furthermore, in order to reduce the thermal contact resistance (air gap) that it is formed between the two surfaces (skin and strut) it was necessary to apply a load between the panel and the strut. In the first instance, bending the strut to form a low curvature fixing and wrapping the skin over it achieved this (two bending positions of 2.5 cm and 5 cm were studied). In the second instance, the panel was examined at various loadings – pressures.

In contrast to the work on Al parts, it was found that the thin CFRP skin (i.e. 2mm) over the CFRP strut could be imaged satisfactorily without significant loading. In the case of the 4mm CFRP skin over the CFRP strut various pressures were applied (similar way to the Al case). In addition, due to the relatively low thermal conductivity of the CFRP material the thermal images during the cooling down process were acquired with a frame rate of 7.49 frames per second (for the 2mm skin) and 3.75 frames per second (for the 4mm skin).

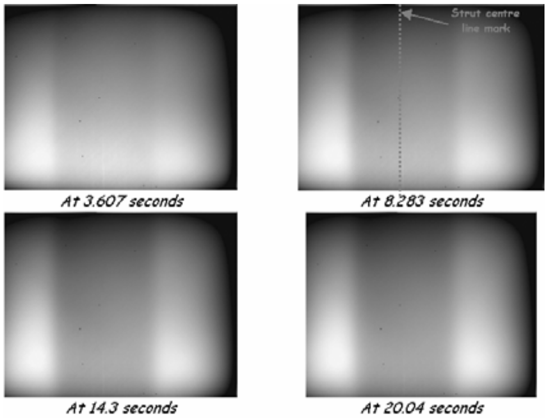

At 3.607 seconds At 8.283 seconds

At 14.3 seconds At 20.04 seconds

Figure 1: a selection of thermal images showing the strut beneath the 2mm CFRP skin

Furthermore, in all cases, 5 line profiles along the X-axis at 20, 74, 128, 182 and 236 (Y pixel values) were taken in order to define the centre of the strut using the FWHM (Full Width Half Maximum) approach.

In this part, the characteristics of thermal images for the assessment of under skin structures of different skin thickness were investigated through modelling, as well as experimentally. PT showed that can be used effectively in the detection of subsurface features located beneath relative thin skins (i.e. up to 4mm). In addition, it showed great potential as far as locating the centre of a substrate accurately. The accuracy of centre line of the subsurface struts for both studied cases was better than 1 pixel (i.e. less than 0.5 mm). This is the limit imposed by the field of view and pixels of the infrared camera (320 x 256).

## 3. Defect detection under multi-ply composite repairs

In PT, the qualitative thermal images can be translated into quantitative results by analysing the time and spatial dependency of the surface temperature. Thus, information concerning the size of a detected defect can be achieved. However, PT is an inherently near surface technique whose effectiveness decreases with defect depth and it is also dependent on the thermal properties of the investigated material.

In this part, a composite repair patch [14] was investigated both experimentally and by modelling, with the intention of assessing an artificially introduced delamination (Teflon). The patch was a 6-ply boron epoxy composite material that was applied on an Al 2024-T3 surface. The dimensions of the Teflon were 25 x 25 mm and it was positioned between the 3rd and 4th ply of the composite patch (120 mm long x 70 mm wide). The thickness of each ply was 125 μm.

Experimentally the panel was investigated using the Thermoscope system with the same set-up configuration as in the previous section. For the purposes of thermal modelling, the ThermoCalc-3D software was employed.

In figure 2, a thermogram with representative line profiles from the investigated panel are presented. The delamination was detected by thermography. Line profiles (on both axes) at various times from the obtained thermal images were plotted in order to obtain information about the size of the delamination in relation to the thermal transient time (e.g. possible shrinkage due to thermal diffusion). From the line profiles it was possible to calculate the delamination (figure 3) employing the FWHM approach.

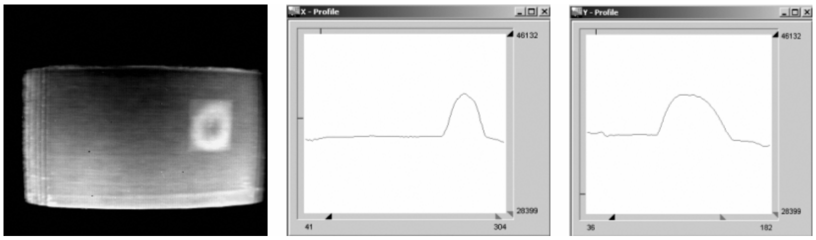

Figure 2: thermogram and representative line profiles of the investigated composite panel

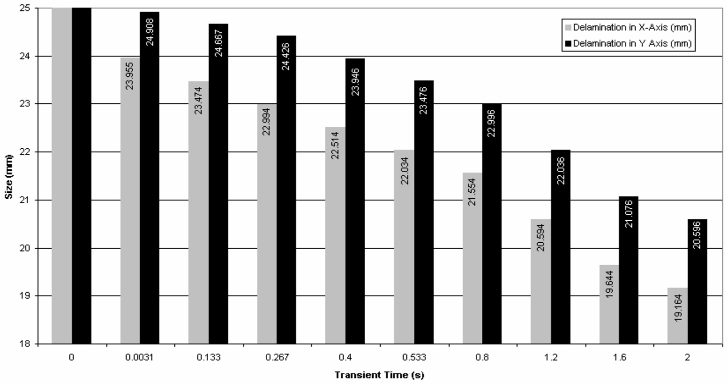

Figure 3: Size –vs- thermal transient time graph of delamination in composite patch.

Thermal images, spatial profiles and thermal contrast curves of the panel from the thermal modelling run are presented in figure 4. The results give a good indication of how the composite material responds to thermal heating. It shows the behaviour of a delaminated composite material after it was heated with a thermal excitation source uniformly in order to detect a sub-surface defect by means of PT.

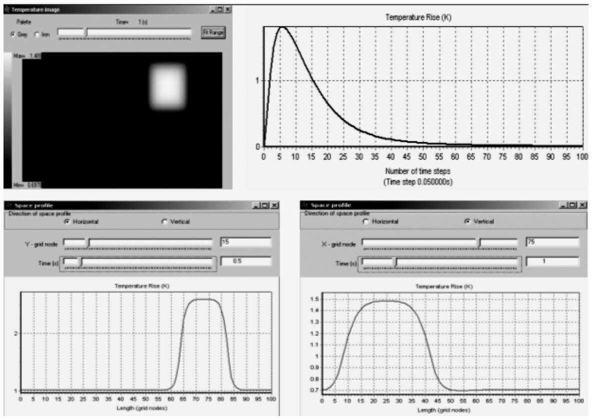
Temperature image

Palette ● Grey ○ Iron

Time= 1 [s]

Space profile

Direction of space profile ● Horizontal ○ Vertical

Y - grid node 15

Time [s] 0.5

Space profile

Direction of space profile ○ Horizontal ● Vertical

X - grid node 75

Time [s] 1

Figure 4: thermal modelling results of composite panel. Upper graph shows development of contrast, Delta T, over defect with time. A thermal image and spatial profiles in both axes (X and Y) are also shown.

Therefore, from the obtained results it is shown that experimentally or by the use of thermal modelling it is possible to evaluate (qualitatively and quantitatively) near surface delaminations in composites.

## 4. Impact damage on CFRP panels and honeycomb sandwich structures

Damage caused by low velocity impacts is a particular concern in the aircraft industry. In this work, impact damaged CFRP panels (150 x 100mm) of 2mm thickness (16 ply with a quasi-isotropic lay-up), as well as sandwich composite samples formed after bonded to the two faces of 25 mm thick Type 6 Nomax honeycomb core were investigated. All panels were cut from the same sheet. A falling weight impactor with a hemispherical 12.5 mm radius head was used to apply impacts of controlled energy. During impact, the samples were supported around their edges over a 125 x 75 mm aperture, allowing the bulk of the panels to rebound freely on impact. The Thermoscope pulsed transient thermographic system, employing the medium wave infrared camera (Merlin 3-5 μm by Indigo), was used to image the impact damage [15].

PT is a rapid large area technique with the additional advantages of being single-sided and non-contact. These attributes make this technique particularly suitable for surveying either single panel or sandwich structures for impact damage. Examples of thermography images impact damage in the two types of samples are shown in figure 5.

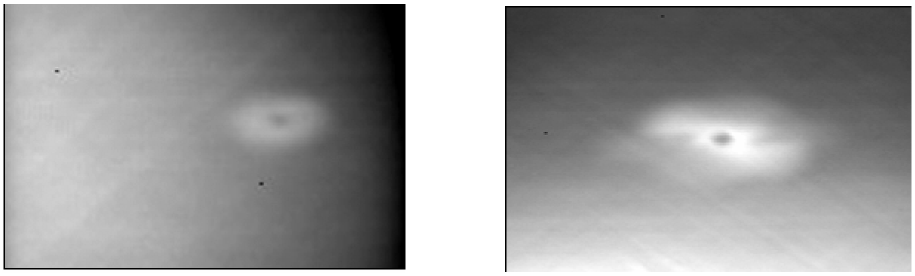

Figure 5: thermal images of 12.75J impact damage in a panel sample (left) & in a sandwich sample (right) taken 0.5s after flash heating.

In addition to the evident difference in defect size, the sandwich sample image contains a high contrast component caused by a delamination close to the surface. A comparison of contrast vs. elapsed time for the two images shows contrast peaking at a much earlier time for the sandwich sample, consistent with delaminations close to the surface.

The size and the through thickness characteristics of the impact damage produced in single panel and sandwich samples are reflected in the NDT images obtained by PT. The technique has been shown to be effective for detecting and imaging impact damage in either isolated panel or sandwich samples.

### 5. Drilling induced defects on multi-ply laminates of carbon fibre composites

An area where relatively little work has been done is on the criticality of defects formed during either manufacturing or assembling of aircraft composites. There are quite a few defects that can occur within composites both due to the manufacturing of the material and subsequent handling and assembly of manufactured components. Such defects can reduce the mechanical performance of the structure and thus must be studied. Knowledge of defects, their detection and their importance is important in cutting manufacturing costs and thus it is of particular significance to the aerospace industry.

In this work, multi-ply laminates of HEXCEL AS4/8552 carbon fibre composites containing drilling induced defects were examined [4]. 4mm thick laminates that were produced by the lay-up of 16 plies of UD-prepreg tape in a predetermined sequence were tested. The lay-up sequence was a quasi-isotropic (25/50/25) laminate with a stacking sequence of: [(45,0,-45,90)2]s.

Various assembly defects were introduced to the CFRP panels using specific drilling parameters, i.e. spindle speed, feed rate, clamping and backing. The defects were all associated with the drilling of holes within composite panels. PT, one of the latest non-destructive techniques used effectively for the assessment of aircraft materials, was employed in the imaging of the artificially created defects. In particular, the following assembly related types of defects were investigated:

- Overtorqued fasteners: through thickness crushing of material due to loads imposed by the fastener.
- Burned drilled holes: localised damage in region of drilled hole caused by frictional heating of drill bit.
- Mislocated – podged holes: holes produced in incorrect location for fastener.
- Over-countersunk holes: countersink drilled at incorrect angle.

PT was carried out to evaluate the quality around the drilled hole, as well as the defect size. The Thermoscope pulsed thermographic system employing the medium wave (3 – 5 μm) infrared camera (Indigo) was used for the imaging of the defected samples. The pulsed thermographic investigation was made of the dependence of defect image contrast and of thermal properties of the tested materials.

The overtorqued fasteners' defects might arise at any section on a CFRP panel where bolts are used to fasten together two components. This overtorquing of fasteners can result in damage to the composite in the region local to the bolt-hole through the thickness of the laminate. The extent and severity of a defect is greatly dependent on the loads induced through the thickness of the examined composites.

Figure 6a, shows a minor defect within the investigated panel. The drilled hole can be seen as a dark circular region (lower temperature) in the centre of the thermal image. A very thin bright grey area (higher temperature) can just be seen around the drilled hole, indicating the presence of a defect. Figure 6b displays the thermal image of the panel enclosing a typical defect. Although the thermal image appears to be analogous to that of figure 6a, nonetheless, the hot area around the drilled hole is slightly more distinctive, suggesting greater damage in the form of matrix cracking and/or delaminations. Figure 6c displays the severe crushed material defect. The damage region appears to spread further from the edge of the hole and looks to be more severe. Nonetheless, the damage does not seem to be continual around the perimeter of the drilled hole and that the area adjacent to the drilled hole appears to be defect free.

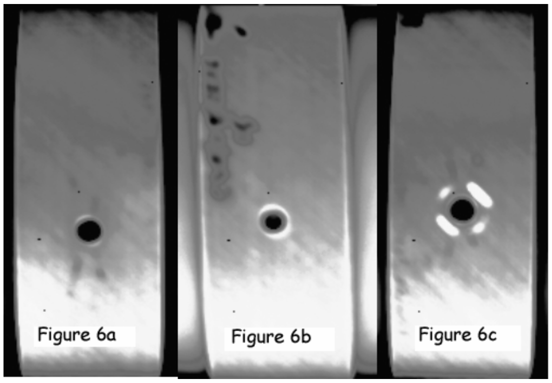

Figure 6: Thermal Images of samples with overtorqued fasteners' defects.

The burned drilled holes' defect, which is a result of the localised frictional heating between the drill bit and the composite material, was also investigated. This type of defect can be detected macroscopically within the drilled hole and is likely to exist throughout the thickness of the material, being most severe towards the through thickness centre of the laminate. Similarly, the acquired thermal images indicated the extent of the damage on the investigated panels.

The mislocated - podged holes' defect occurs in assemblies where several fasteners are utilised to attach a component in place. Several times, the misalignment of the drilled hole is considerably great that makes it impossible for the fastener to be inserted; podging of such holes involves inserting an object, i.e. screwdriver, into the misaligned hole and levering the holes into position. In CFRP, such process has the potential to induce severe damage in and around the drilled hole. PT was used effectively to obtain information on the extent of damage due to podged holes.

The use of countersunk bolts is common within aircraft applications. However, a number of different defects can occur when drilling countersunk holes, i.e. countersunk hole is drilled too deep causing the bolt head to sink below the aerodynamic surface of the component. Moreover, an overcountersunk hole is not easily repaired and since countersinking removes material from around the hole, such defects can potentially be detrimental to the mechanical performance of the component. PT was competent in the detection of overcountersunk holes.

## 6. Conclusions

The main objective of this work was to study the effectiveness of PT to assess various defects and or features on representative aerospace materials. The technique provided excellent results in all cases. The advantages of the technique are that it investigates rapidly large areas for surface or near surface defects and that it generates interpretable results. Nonetheless, a major disadvantage is that its success is highly dependent on defect depth and size, which restricts its application to near surface defect imaging.

## 7. Acknowledgements

Acknowledgements are attributed to the Hellenic Aerospace Industry for the preparation of the composite patches, to Airbus UK for providing the HEXCEL AS4/8552 carbon fibre composites and the aluminium alloy skin and along with EPSRC for their financial support concerning the carbon fibre composites research project and to Westland Helicopters for the supply of the sandwich core materials. The authors would also like to thank the EU (5th Framework Programme – AHEAD) for providing the Thermoscope system.

## REFERENCES

1. MALDAGUE (X.). - *Applications of Infrared Thermography in NonDestructive Evaluation.* Rastogi (P.K.), Inaudi (D.) eds., Trends in optical nondestructive testing, Elsevier Science, 2000.
2. AVDELIDIS (N.P.), MOROPOULOU (A.). - *Review Paper: Applications of infrared thermography for the investigation of historic structures.* Journal of Cultural Heritage, Vol. 5, No. 1, 2004, p. 119-127.
3. SHEPARD (S.M.). - *Introduction to active thermography for non-destructive evaluation*. Journal of Anti-Corrosion Methods and Materials, Vol. 44, 1997, p. 236-239.
4. AVDELIDIS (N.P.), HAWTIN (B.C.), ALMOND (D.P.). - *Transient thermography in the assessment of defects of aircraft composites*. Journal of NDT & E International, Vol. 36, 2003, p. 433-439.
5. ALMOND (D.P.), PENG (W.). - *Thermal imaging of composites*. Journal of Microscopy, Vol. 201, 2001, p. 163-170.
6. VAVILOV (V.P.), TAYLOR (R.). - *Theoretical and practical aspects of the thermal NDT of bonded structures*. London, Sharpe (R.). ed., Research Techniques in NDT, Vol. 5, Academic Press, 1982.
7. CILIBERTO (A.), CAVACCINI (G.), SALVETTI (O.), CHIMENTI (M.), AZZARELLI (L.), BISON (P.G.), MARINETTI (S.), FREDA (A.), GRINZATO (E.). - *Porosity detection in composite aeronautical structures*. Journal of Infrared Physics & Technology, Vol. 43, 2002, p. 139-143.
8. MALDAGUE (X.), GALMICHE (F.), ZIADI (A.). - *Advances in pulsed phase thermography*. Journal of Infrared Physics & Technology, Vol. 43, 2002, pp. 175-181.
9. SAKAGAMI (T.), KUBO (S.). - *Applications of pulse heating thermography and lock-in thermography to quantitative nondestructive evaluations*. Journal of Infrared Physics & Technology, Vol. 43, 2002, p. 211-218.
10. LUDWIG (N.), TERUZZI (P.). - *Heat losses and 3D diffusion phenomena for defect sizing procedures in video pulse thermography*. Journal of Infrared Physics & Technology, Vol. 43, 2002, p. 297-301.
11. AVDELIDIS (N.P.), ALMOND (D.P.). - *Through skin sensing assessment of aircraft structures using pulsed thermography*. Journal of NDT & E International, Vol. 37, 2004, p. 353-359.
12. KRAPEZ (J.C.), LEPOUTRE (F.), BALAGEAS (D.). - *Early detection of thermal contrast in pulsed stimulated thermography*. Journal De Physique, Vol. 4, 1994, p. 47-50.

13. AVDELIDIS (N.P.), ALMOND (D.P.). - *Transient thermography as a through skin imaging technique for aircraft assembly: modelling & experimental results*. Journal of Infrared Physics & Technology, Vol. 45, 2004, p. 103-114.
14. AVDELIDIS (N.P.), MOROPOULOU (A.), MARIOLI-RIGA (Z.P.). - *The technology of composite patches and their structural reliability inspection using infrared imaging*. Journal of Progress in Aerospace Sciences, Vol. 39, 2003, p. 317-328.
15. AVDELIDIS (N.P.), ALMOND (D.P.), DOBBINSON (A.), HAWTIN (B.C.), IBARRA-CASTANEDO (C.), MALDAGUE (X.). - *Invited Review Paper: Aircraft composites assessment by means of transient thermal NDT*, Journal of Progress in Aerospace Sciences, Vol. 40, 2004, p. 143-162.

Proc. Vth International Workshop, Advances in Signal Processing for Non Destructive Evaluation of Materials
Québec City (Canada),2-4 Aug. 2005. © X. Maldague ed., É. du CAO (2006), ISBN 2-9809199-0-X

# A Combined integral transform asymptotic expansion method for the characterization of interface flaws through stimulated infrared thermography

by A. Bendada

*Department of Electrical and Computer Engineering, Université Laval, Quebec City (Quebec) G1K 7P4 Canada*

## Abstract

This work is devoted to the nondestructive evaluation of materials using stimulated infrared thermography. The proposed approach provides simple analytical solutions to evaluate the lateral extent, and the thickness of a plane flaw in a three-dimensional (3D) heat transfer configuration. It is based on the application of a Laplace transform on the time variable *t*, then a double Fourier transform on the space variables *x* and *y*. Reduction of the models are obtained through an asymptotic expansion method. This mathematical formalism leads to the construction of explicit relationships that are very convenient for quantitative inversion. An experimental validation is performed on a calibrated carbon-epoxy laminate.

**Keywords:** stimulated infrared thermography, nondestructive evaluation, 3D heat transfer, quantitative inversion, composite material.

## 1. Introduction

Complex manufacturing processes of laminated composites increase the risk of flaw appearance whose consequences may be very crucial. In most cases, the control of their quality is needed to be nondestructive in order to allow inspection during different times of the parts life. In this quality investigation, methods based on heat transfer may be very effective. Pulsed infrared thermography is one of the approaches that may be used for that purpose. In this technique, the composite sample is irradiated by a uniform heat pulse on one face while the transient temperature either on the same face or on the opposite one is recorded using an infrared camera. The temperature difference between the pixel of interest on the infrared frame and a reference area considered sane on the same frame represents a signature of the subsurface flaw. It is this signal, usually called the contrast thermogram, which is commonly used to detect and quantify the flaw. In the current work, we propose a new modeling approach based on the use of the 3D thermal quadrupole method [1]. Three-dimensional thermal quadrupoles are obtained by applying to the real temperature field Laplace and Fourier transforms. Air delaminations in stratified composites are thermally characterized by a thermal contact resistance. When this resistance is small compared with the material whole resistance, a perturbation method [2] can be combined with the thermal quadrupole formalism to yield simple analytical solutions of the nondestructive experiment [3]. The perturbation procedure is based on an asymptotic expansion of the physical field versus a small parameter intervening in the model.

## 2. Formulation of the forward problem

The case of a rectangular *(L x ℓ)* flat sample of thickness *e* that contains a resistive flaw of finite width *a* and finite length *b*, with a uniform contact resistance *R* on its whole area, is typical of a delamination in a composite material (Figure 1). In a typical pulsed infrared thermography test, one can assume that: the thermal excitation of the sample is a Dirac pulse characterized by a uniform absorbed energy *Q* (at time *t = 0*); the front face of the sample is adiabatic; and the sample temperature is zero before excitation.

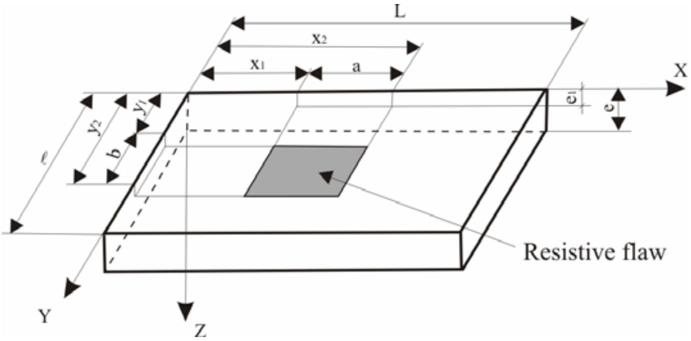

Figure 1. Geometric sketch of a limited extent flaw within an anisotropic material.

The Laplace transform $\tau(x, y, z, p)$ (where $p$ is the Laplace variable) of the temperature $T(x, y, z, t)$ in the sample is the solution of the following set of equations:

$$\frac{\partial^2 \tau}{\partial z^2} + \frac{\lambda_x}{\lambda_z}\frac{\partial^2 \tau}{\partial x^2} + \frac{\lambda_y}{\lambda_z}\frac{\partial^2 \tau}{\partial y^2} - \frac{p}{a_z}\,\tau = 0 \tag{1a}$$

$$x = 0, L \quad \rightarrow \quad \frac{\partial \tau}{\partial x} = 0 \tag{1b}$$

$$y = 0, l \quad \rightarrow \quad \frac{\partial \tau}{\partial y} = 0 \tag{1c}$$

$$z = 0 \quad \rightarrow \quad -\lambda_z \frac{\partial \tau}{\partial z} = Q \tag{1d}$$

$$z = e_1 \quad \rightarrow \quad \frac{\partial \tau^{\sup}}{\partial z} = \frac{\partial \tau^{\inf}}{\partial z} \tag{1e}$$

$$\tau^{sup} - \tau^{inf} = R\, s(x, y) \left[ -\lambda_z \frac{\partial \tau}{\partial z} \right] \tag{1f}$$

$s(x, y) = 1$ *if* $(x, y) \in \{[x_1, x_2] \times [y_1, y_2]\}$ and $s(x, y) = 0$ elsewhere

$$z = e \quad \rightarrow \quad \frac{\partial \tau}{\partial z} = 0 \tag{1g}$$

This forward problem has already been solved elsewhere by the author [3], using 3D thermal quadrupoles and mathematical perturbations. Here, only pertinent results are recalled. After application of a double Fourier transform (along *x* and *y* directions) on the Laplace temperature distribution $\tau(x, y, z, p)$, it was shown that the thermal contrast on the rear face (non-irradiated face) could be written under the following form (for small *R*-values):

$$\Delta\theta = -\,R\frac{4}{\alpha\beta}K\frac{\sinh(u\,e_1)\,\sinh(\sqrt{p}\,(1-e_1))}{\sinh(\sqrt{p})\,\sinh(u)} \qquad (2)$$

where $K = \sin\left(\alpha\frac{x_2-x_1}{2}\right)\cos\left(\alpha\frac{x_1+x_2}{2}\right)\sin\left(\beta\frac{y_2-y_1}{2}\right)\cos\left(\beta\frac{y_1+y_2}{2}\right)$

$\alpha$ and $\beta$ are the Fourier variables, and $u = \left(p+\alpha^2+\beta^2\right)^{1/2}$

Return from the new $(\alpha, \beta, p)$ domain to the original $(x, y, t)$ domain can be achieved numerically by using Fast Fourier Transform (FFT) and Stehfest [4] algorithms.

### 3. Explicit inversion of the lateral extent and thermal contact resistance

In this section, we show how the lateral extent of the flaw can be derived from the space averaging of the Laplace contrast distribution $\Delta\tau(x, y, z_s, p)$ when the depth of the flaw $e_1$ is already known. The space average of the Laplace contrast distribution is defined as:

$$\Delta\bar{\tau} = \frac{1}{L\ell}\int_0^L\int_0^\ell \Delta\tau(x,y,z_s,p)\,dx\,dy \quad ; \quad \text{with } z_s = 1 \text{ (rear face)} \qquad (3)$$

Processing of Equation 2 for $\alpha=\beta=0$ allows the calculation of $\Delta\bar{\tau}$ for the rear face:

$$\Delta\bar{\tau} = -R\frac{a\,b}{L\,\ell}\frac{\sinh(\sqrt{p}\,e_1)\sinh\left\lfloor\sqrt{p}(1-e_1)\right\rfloor}{\sinh^2(\sqrt{p})} \qquad (4)$$

This shows that the average Laplace contrast (and therefore the averaged contrast $\Delta\bar{T}$ in the original space) is proportional to the product of the area *(a x b)* and the thermal resistance *R* of the flaw. To be able to estimate the lateral extent of the flaw, the thermal resistance *R* must be independently estimated. A one-dimensional (1D) inverse technique suitable for wide enough delaminations [5] could be used to estimate *R* above the center $(x_c, y_c)$ of the defective area. If $n_1$ and $n_2$ denote the experimental Laplace contrasts on the rear face upon the center of the flaw, the thermal resistance is given by the following relationship:

$$R = \frac{n_1^2\sinh(\sqrt{p_1})\tanh(\sqrt{p_1})}{n_2\cosh(\sqrt{p_1})-n_1} \qquad (5)$$

where $n_i = \Delta\tau(x_c, y_c, 1, p_i)$, $i = 1, 2$ and $p_2 = 4\,p_1$

In the case of a flaw of small resistance *R*, application of Equations 4 and 5 allows the determination of the flaw extent if its depth $e_1$ is known is *a priori* known.

## 4. Experimental validation

### 4.1. Measurement technique

The test sample is a square slab *60 mm x 60 mm* and *2-mm*-thick, made out of a 14-layer carbon-epoxy laminate. The material is orthotropic and its thermal properties are: $\lambda_z = 0.67\ W\ m^{-1}\ K^{-1}$, $\lambda_x = \lambda_y = 2.40\ W\ m^{-1}\ K^{-1}$, $\rho c = 1.62\ 10^{-6}\ J\ m^{-3}\ K^{-1}$. The delamination is simulated with a *10 mm x 10 mm* square artificial insert made out of two 25-µm-thick Teflon® films. These inserted films simulate a 3-µm-thick air delamination located at mid-depth in the sample ($e_1 = 0.5$). Heat pulse excitation is produced by an assembly of four flash tubes. Each flash tube is located on one side of a *10 cm x 10 cm* square frame. The duration of the photothermal excitation is less than *5 ms* for an incident energy $Q$ of *3* to *4* $J\ cm^2$. The temperature change on the rear face of the sample after the flash heating is recorded with a Thermovision 782 SW Agema infrared camera connected to a computer system controller. The optical scanning gives a scan rate of 25 images per second and an image resolution of 128 pixels by 64 lines; the thermal resolution is around *0.08 °C*.

### 4.2. Results

An instantaneous infrared frame of the rear face shows the flaw region on Figure 2. Application of Equation 5 with $p_1=1$ at the level of the defect center, leads to the following value of the normalized flaw thermal resistance $R = 0.185$. This value is almost three times higher than the nominal value corresponding to the Teflon® films. Previous experiments on similar calibrated samples showed that air layers of few micrometers trapped between the Teflon® films or between the films and the composite matrix are sufficient to justify this deviation.

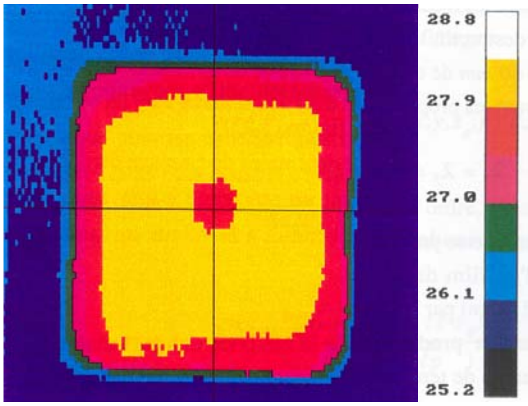

Figure 2. Infrared image at time $t = 1.4\ s$ after the flash heating in a rear face experiment.

Application of Equation 4 with the preceding value of $R$, and $e_1 = 0.5$, can yield a value for the area *(a x b)* once a value has been chosen for the Laplace variable $p$. The optimal value of $p$ was found to be equal to *6*. Since our modeling does not take into account the lateral heat losses, the integration domain has been reduced to overcome the edge effects ($L \times \ell$ = 48 mm x 42 mm, instead of 60 mm x

60 mm). The experimental Laplace contrast field (for $p = 6$) was calculated; a profile of this contrast crossing the center of the defect is reported on Figure 3.

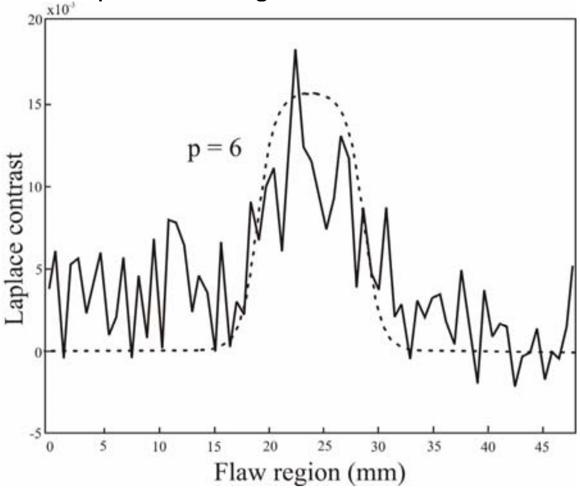

Figure 3. Experimental and theoretical Laplace profiles across the defective region.

The signal is disturbed with a great amount of measurement noise. The corresponding average value of the Laplace contrast is $\Delta\bar{\tau} = -18 \text{ x } 10^{-4}$. Since $a = b$, the estimated value of $a$ using Equation 4 is *8.9 mm*, which represents a discrepancy of – 11% with respect to the nominal value. A simulated Laplace contrast distribution calculated with $p = 6$, $e_1 = 0.5$, $a = b = 10$ *mm,* and $R = 0.185$ is obtained using Equation 5 and the inverse Fourier transform; it is plotted in Figure 4. A theoretical Laplace profile above the center of the defective region is derived from the latter figure and reported in Figure 3 together with the experimental profile. The theoretical profile shows that the region affected by the Laplace contrast is approximately *20 x 20* $mm^2$, which is not the case for the experiment where noise spreads outside this zone. It should be pointed out however that even with the highly noisy data; the proposed inversion approach has led to an appropriate estimation for the flaw parameters.

## 5. Conclusion

Unsteady three-dimensional heat diffusion within an anisotropic material containing a limited extent discontinuity has been solved using a perturbation expansion and integral transforms. Parameter estimation procedures based on the solutions obtained via perturbations method and 3D thermal quadrupoles have been implemented. The theoretical results were then validated on an artificial sample submitted to a pulsed thermography test. The flaw was composed by the superimposition of two thin Teflon® films. The estimated lateral extent of the flaw was very close to the nominal value. However, the flaw thermal resistance was more than twice higher than the nominal value. This was explained by air layers trapped between the Teflon® films or between the Teflon® films and the matrix of the composite material.

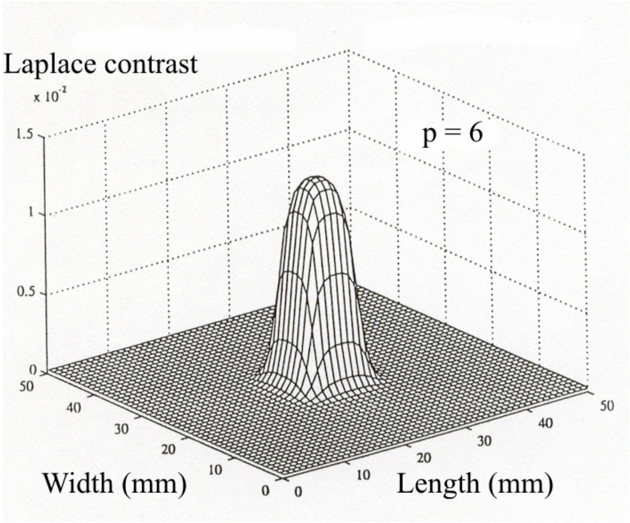

Figure 4. Theoretical Laplace distribution calculated for a depth $e_1 = 0.5$, a lateral extent $a \times b = 10$ mm x 10 mm, and a thermal resistance $R = 0.185$.

## REFERENCES

[1] Maillet (D.), André (S.), Batsale (J.C.), Degiovanni (A.) and Moyne (C.). - *Thermal quadrupoles: solving the heat equation through integral transforms*. Chichester, Whiley, 370 p., 2000.
[2] Aziz (A.) and Na (T.). - *Perturbations Methods in Heat Transfer*. Berlin, Springer-Verlag, 1984.]
[3] Bendada (A.). - *Approximate solutions to three-dimensional unsteady heat conduction through plane flaws within anisotropic media using a perturbation method.* Modeling and Simulation in Material Science and Engineering, vol. 10, 2002, p. 673-684.
[4] Stehfest (H.). - *Remarks on Algorithm 368, Numerical Inversion of Laplace Transforms.* Commun. ACM, vol. 13, 1970, p. 47-49.
[5] Maillet (D.), Batsale (J.C.), Bendada (A.), Degiovanni (A.). – *Integral methods and nondestructive testing through stimulated infrared thermography.* International Journal of Thermal Science, vol. 35, 1996, p. 14-27.

Proc. Vth International Workshop, Advances in Signal Processing for Non Destructive Evaluation of Materials
Québec City (Canada),2-4 Aug. 2005. © X. Maldague ed., É. du CAO (2006), ISBN 2-9809199-0-X

# Inversion of microscopic lock-in thermograms in the presence of emissivity contrast

by O. Breitenstein[1] and F. Altmann[2]

[1]*Max Planck Institute of Microstructure Physics, Weinberg 2, D-06120 Halle, Germany;* [2]*Fraunhofer Institute for Mechanics of Materials, Heideallee 19, D-06120 Halle, Germany*

## Abstract

None of the conventionally displayed images of lock-in thermography (in-phase or 0° image, out of phase or -90° image, amplitude image, phase image) is able to become inverted in the presence of emissivity contrast. The phase signal is inherently emissivity-corrected, but here contributions of different heat sources superimpose very nonlinearly, which prevents any meaningful deconvolution. It is shown that the "0°/-90°" image, as an alternative kind of representation of lock-in thermography images, being also inherently emissivity-corrected, is able to be inverted for obtaining e.g. the lateral power distribution in an electronic device. Blackening the surface by colloidal bismuth also may remove the emissivity contrast.

**Keywords:** lock-in thermography, emissivity, image inversion, deconvolution, electronic devices

## 1. Introduction

Lock-in thermography (LIT, often also called thermal wave imaging), which is a very successful technique in non-destructive evaluation (NDE) since many years [1], was in the last years increasingly used for failure analysis in electronic devices [2, 3]. The goal of electronic device failure analysis is not to detect subsurface structures, as for NDE, but rather to image electrically activated local heat sources in these devices. Until now LIT has been used successfully e.g. for investigating shunts in solar cells and for failure analysis (FA) of integrated circuits (ICs). Many types of failures in ICs, like gate oxide brakdowns, latchups, or line shorts, are leading to local heat sources, if the supply voltage is applied to the device. Even the normal operation of these devices is leading to internal electrically stimulated local heat sources. Therefore, microthermal inspection has been a standard FA tool for IC inspection since many years. Until recently only techniques like liquid crystal microscopy [4] or fluorescent microthermal imaging (FMI) [5] have been used in this field, rather than infrared (IR) imaging. There are two main reasons for that: 1. The spatial resolution of thermal IR imaging is limited by the used wavelength of typically 3-5 µm to the order of 5 µm. 2. The IR images are heavily corrupted by the so-called 'emissivity contrast'. Note that the top layers of ICs are partly covered with metal lines, which show a much smaller IR emissivity than the surrounding silicon material. Thus, these lines appear dark in an IR image, compared to the surrounding silicon material of the same temperature, and this 'emissivity contrast' often dominates over the actually interesting thermal contrast.

The introduction of lock-in thermography (LIT) shows a dramatic improvement of the detection sensitivity and opens new possibilities to correct for the emissivity contrast, as compared to steady-state thermography. For example, the phase image, which is actually a measure of the time delay of the periodic temperature modulation compared to the applied voltage pulses, is inherently emissivity-corrected. Thus, in the presence of emissivity contrast, the phase image is much more meaningful for imaging internal local heat sources than the amplitude image. LIT is about two orders of magnitude more sensitive than previous microthermal FA techniques [4,5], therefore LIT has gained new interest in the FA community, in spite of its limited spatial resolution.

Another general problem of thermal analysis is the thermal blurring effect, which is due to the inevitable lateral heat conductivity in the investigated material. Though, due to the dynamic nature of LIT, lateral heat diffusion is already suppressed in LIT to a certain degree, especially for microscopic investigations the thermal blurring often still disturbs. Note that the characteristic decay length of thermal waves is the thermal diffusion length $\Lambda$, which is about 1 mm in silicon for a typical lock-in frequency of 30 Hz and is reducing with $1/\sqrt{f_{lock\text{-}in}}$ [6]. Especially for microsocopic investigations, having a pixel resolution below 10 µm, the detected thermograms may considerably deviate from the acually interesting lateral power density distribution. This blurring effect may be reduced by working at higher lock-in frequencies, which, however, is always technically limited.

Mathematically, the blurring effect can be described by a convolution process. The (complex) temperature response T(x,y) around a certain (real) lateral power distribution P(x,y) is given by a mathematical convolution between this power distribution and the 2-dimensional (complex) point spread function PSF(x,y) [2,3]. If this PSF is known, the power distribution may be calculated from the measured lock-in thermography image T(x,y) by applying an appropriate image deconvolution procedure. This procedure is also called 'inversion', since it inverts the thermal blurring effect. In this contribution, first we present some simulations, showing that the inversion of conventional lock-in thermograms is not meaningful in the presence of emissivity contrast. Even the phase image, which is inherently emissivity-corrected, is not able to become inverted, since it depends very non-linearly on the power of different heat sources. Then we show that the '0°/-90°' image, as a special kind of representing LIT images, is able to become inverted for microscopic applications, even in the presence of emissivity contrast. Finally, we are presenting a novel technique of blackening the surface of ICs for removing the emissivity contrast.

## 2. Experimental

All LIT results shown in this contribution were obtained by using the TDL 384 M 'Lock-in' thermography system by Thermosensorik GmbH (Erlangen). This LIT system is based on a Stirling-cooled 384x288 pixel mercury-cadmium-telluride focal plane array, which is working in the mid IR range (3-5 µm) and shows a room temperature noise level (NETD) of 20 mK at a full frame rate of 120 Hz. For performing microscopic investigations, it may be equipped with a x2.5 or a x5 microscope objective, leading to a pixel resolution of 10 µm and 5 µm, respectively. This system is working in synchronous operation mode, hence the lock-in trigger is derived from the frame trigger of the free-running IR camera. The modulation of the internal heat sources in the investigated devices is performed by periodically pulsing the supply voltage of the devices (on and off) with a duty cycle of 1:1. The lock-in correlation is performed as a two-phase sine / cosine correlation on-line with the resulting image being updated and displayed every 10 seconds. The system allows to display one of the primary signals (in-phase / 0° signal or out-of-phase / -90° signal) or the amplitude or the phase signal at choice. A constant systematic phase error may be corrected.

The simulations and deconvolutions presented here were performed by using the DECONV software, which was developed by the authors [3]. This software allows to simulate any type of lock-in thermogram from a given lateral power distribution, which may be at the surface or at a constant depth of the sample. The sample may be assumed to be either infinitely thin, infinitely thick, or to have a well-defined constant thickness, but it is assumed to be laterally and depth-homogeneous. For a finite sample thickness, the calculation includes mirror heat sources to account for the two surfaces. The main task of the DECONV software is to deconvolute measured or simulated lock-in thermograms by using two alternative approaches, which are the Fast Fourier Transform (FFT) based deconvolution and the Constraint Iterative technique, for details see [2,3]. In both cases, a compromise between the acheaved spatial resolution and the inevitable degradation of the signal-to-noise ratio may be chosen. A regularisation (noise reduction) procedure for the input images by using a Wavelet or a JPEG based procedure is possible, but was not used for the examples introduced here.

## 3. Simulations

An IC containing microscopic heat sources at the surface can be modelled to a good accuracy as a homogeneous sample of infinite thickness. In this case, the LIT point spread function, which is the thermal response to an oscillating point heat source at the surface, is well-known [6]:

$$\mathrm{PSF}(r,t)=\frac{A}{r}\exp\left(-r\sqrt{\frac{i\,\omega\,c_p\,\rho}{\lambda}}\right)\exp\,(i\,\omega\,t)=\frac{A}{r}\exp\left(\frac{-r}{\Lambda}\right)\exp\left(i\left(\omega\,t-\frac{r}{\Lambda}\right)\right) \tag{1}$$

with $r=\sqrt{x^2+y^2}$ and $\Lambda=\sqrt{\frac{2\lambda}{\rho c_p \omega}}$ (thermal diffusion length)

($r$ = distance from point source, $A$ = amplitude factor; depending on the power, $\omega = 2\pi f_{\text{lock-in}}$, $i=\sqrt{-1}$, $t$ = time, $c_p$ = specific heat, $\rho$ = density, $\lambda$ = heat conductivity). The local in-phase (or 0°) contribution of the PSF, which is most appropriate for deconvolution [2], is according to (1):

$$\mathrm{PSF}^{0^\circ}(x,y)=\frac{A}{\sqrt{x^2+y^2}}\;\exp\left(\frac{-\sqrt{x^2+y^2}}{\Lambda}\right)\cos\left(\frac{-\sqrt{x^2+y^2}}{\Lambda}\right) \tag{2}$$

If $\varepsilon(x,y)$ is the lateral distribution of the emissivity (emissivity image), the 0°-image resulting from a LIT measurement of a lateral power distribution $P(x,y)$ calculates to:

$$T_\varepsilon^{0^\circ}(x,y)=\varepsilon(x,y)\int_{x,y}P(x,y)\,\mathrm{PSF}(x-x',y-y')dx'dy' \tag{3}$$

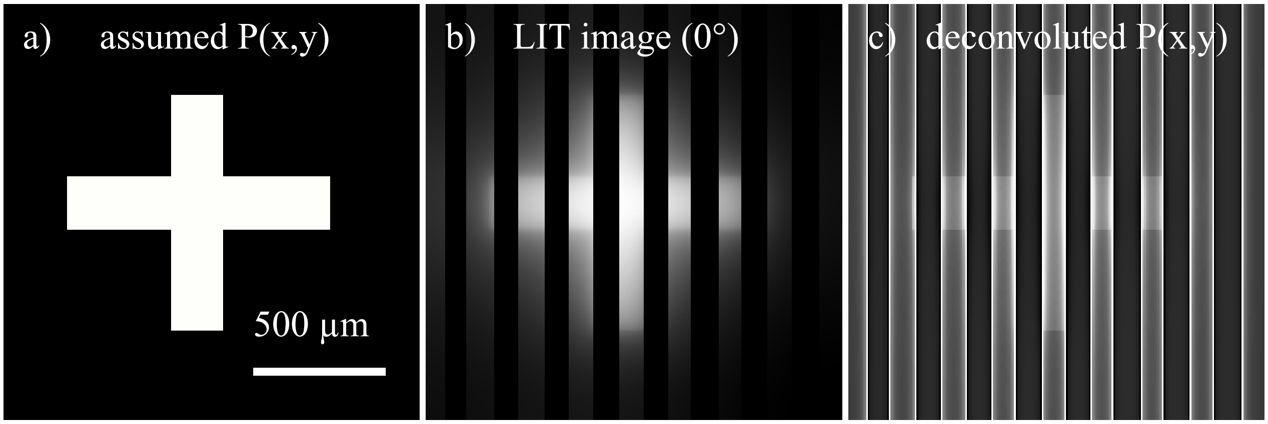

Fig. 1: (a) Assumed power distribution, (b) simulated 0° lock-in thermogram, (c) result of deconvolution

This simulation has been performed assuming a cross-shaped power distribution, $f_{\text{lock-in}}$ = 10 Hz, and an emissivity image consisting from vertical stripes with an emissivity contrast of 1:0.1, which mimic vertical metallic lines at the surface. The result in Fig. 1 shows that the power cross appears blurred in the LIT image, and that the assumed metal lines appear dark, as expected. This image was formally deconvoluted for revealing the power distribution, leading to image (c). While a deconvolution of a thermogram of this power distribution with a homogeneous emissivity of $\varepsilon(x,y) = 1$ exactly revealed the assumed power distribution (a), the result in (c) is strongly corrupted by the emissivity contrast, hence it is nearly meaningless. This simulation demonstrates that, in the presence of a strong emissivity contrast, which is typical for ICs, conventional deconvolution of LIT images does not work. In the following two sections, two solutions to this problem are introduced.

## 4. Deconvolution using 0°/-90° image

The usual way to suppress an emissivity contrast in IR imaging is to cover the surface with a "black" layer having a high and homogeneous emissivity in the wavelength range of the IR camera. However, for inspecting microscopic devices like ICs, this measure is only hardly applicable. The thickness of usual paint layers is between 20 and 200 µm, which is already large against the typical pixel resolution of 5 to 10 µm. Note that only the surface of the black layer emits light, and the heat spreads in all 3 dimensions within the black layer. Therefore the application of this layer would drastically reduce the spatial resolution. The application of an especially thin black layer is described in the following section. The question remains, in which way LIT images of an uncovered IC are able to become deconvoluted. For answering this question, let us first consider the different ways to display LIT images.

The two primary images of a LIT experiment are the 0° and the -90° image, representing the magnitudes of the temperature modulation component being in-phase with the applied bias pulses (the 0° image) and of the component being out-of-phase to the bias pulses (the -90° image). The -90° image is usually chosen instead of the +90° one (which actually would be the imaginary part), since the latter is essentially negative. From these two images, the phase-independent amplitude image A and the phase image $\Phi$ may easily be calculated:

$$A = \sqrt{\left(T^{0°}\right)^2 + \left(T^{-90°}\right)^2} \qquad \Phi = \arctan\left(\frac{-T^{-90°}}{T^{0°}}\right) \tag{4}$$

The conventional way to display LIT results is to use one of these four representations, which show different properties [2]. The 0° image shows the best spatial resolution, which may be much better than the thermal diffusion length $\Lambda$, whereas the resolution of the -90° image is much poorer and in the order of $\Lambda$. If there are different nearby lying heat sources in the device with their thermal signals overlapping, their contributions add up linearly only for these two primary components. The amplitude image A is a vector addition of these components according to (4), hence it also shows a good spatial resolution with a stronger halo around than the 0° image, but here contributions of different heat sources don't add up exactly linearly anymore. The 0°, the -90°, and the amplitude images are all modulated by the emissivity contrast. In contrast, the phase image $\Phi$ shows inherent emissivity correction, since both the 0° and the -90° image are modulated by the emissivity (see (4)). On the other hand, the spatial resolution of the phase signal is only in the order of $\Lambda$, and overlapping contributions of the phase signal add up very nonlinearly. Note that the two basic conditions for the application of image deconvolution are the absence of emissivity contrast and that image contributions from different sources have to add up linearly. According to these two conditions, none of the conventionally displayed LIT images is able to become deconvoluted successfully.

In the following we will shows that the '0°/-90°' image, as another kind of representation of LIT images, can be deconvoluted, at least for microscopic investigations. The 0°/-90° signal is related to the inverse of the phase signal $\Phi$. Like the phase signal, it is inherently emissivity-corrected, but in contrast to this it shows a better spatial resolution, just like the 0° signal. Note that, for a point heat source at the surface, the 0° signal and the amplitude signal are diverging in source position, but the -90° and the phase signal are not. This is the reason for the poor spatial resolution of -90° and phase images. In microscopic regions, hence for lateral distances smaller than $\Lambda$, the thermal -90° signal can be taken to be 'nearly constant'. Since this signal is modulated by the emissivity, the -90° signal is in good approximation proportional to the emissivity, hence the 0°/-90° signal is an 'emissivity-corrected 0° signal'. As such, it can be deconvoluted, as shown below. Moreover, this kind of representation has the advantage of having a much better spatial resolution than the phase signal. So, even if no image deconvolution is intended, it is often more useful to image the 0°/-90° signal than the phase signal.

Fig. 2 shows the 0° image, the -90° image, the 0°/-90° image, and the power image deconvoluted from the 0°/-90° image, of an operational amplifier (µA 741) in normal operation with the supply voltage pulsed at $f_{\text{lock-in}}$ = 10 Hz. The total dissipated power is about 6 mW, the thermal signals are in the order of some mK. While the -90° signal (b) displays essentially the emissivity contrast, in the 0° image (a) a certain inhomogeneity is already visible. However, also this image is dominated by the emissivity contrast. All local heat sources are easily visible in the 0°/-90° image (c), which is perfectly emissivity-corrected. In the deconvoluted power distribution (d) the spatial resolution is further improved, but the signal-to-noise ratio is degraded. This degradation, which is inherent to any kind of image deconvolution, is especially remakable in the very low emissivity region at the bottom left.

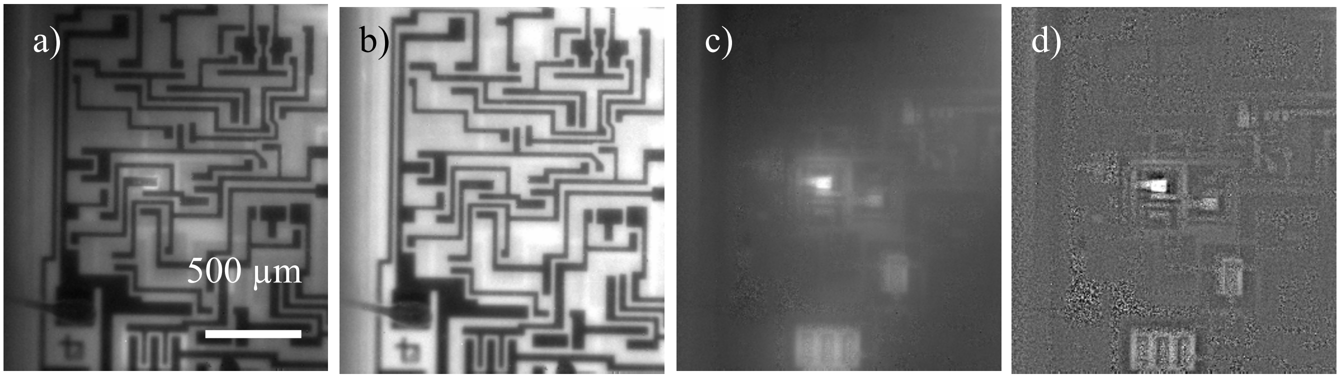

Fig. 2: (a) 0° image, (b) -90° image, (c) 0°/-90° image, and (d) power distribution deconvoluted from (c) of an operational amplifier in normal (pulsed) operation

## 5. Blackening the surface with colloidal bismuth

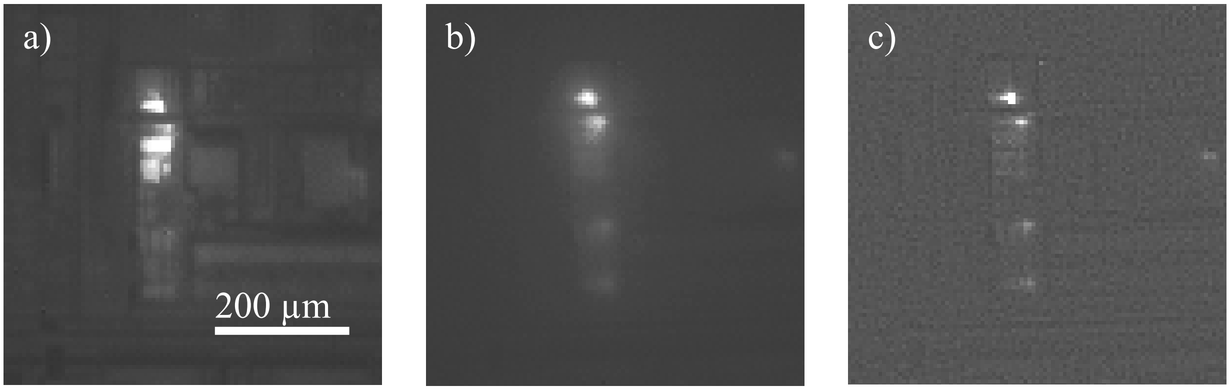

Fig. 3: (a) 0° image of the uncovered surface, (b) 0° image of the blackened surface, and (c) power distribution deconvoluted from (b) of a CMOS IC containing failure-induced heat sources

It was mentioned in the previous section that layers of usual paints are too thick to be applied to microscopic investigations of ICs. It is well known that colloidal metal particles are forming if a metal is evaporated in a residual gas atmosphere. These are good IR absorbers ('silver black' or 'gold black'), which are used in industrial IR detectors [7]. However, these layers are electrically conducting. Therefore they are not appropriate for IC investigation with electrical stimulation, since they would provide a short at the terminals of the IC. We have found that colloidal bismuth is leading to high-ohmic black layers, whose conductivity is not significant anymore after a few days of storage in air [8]. These films are prepared by evaporating 600 mg of Bi from a tantalum evaporation boat within 10 s at a residual air pressure of 200 Pa in a closed evaporation assembly, which provides a radiation shield between the evaporator and the specimen. More details to the preparation of these black thin films can be found in [8]. These films have a thickness of typically 10 µm and provide an absorptance above 80%

in the spectral range of 3 to 5 µm. They consist from fluffily-packed nanoscopic metal flakes, which can easily be removed from the surface in an ultrasonic water bath. Fig. 3 shows a 0° image of the uncovered surface (a), the 0° image of the black surface (b), and the power distribution (c) deconvoluted from (b) of a faulty region in a CMOS IC. Indeed, in the image of the blackened surface, the visible emissivity contrast is removed. Again, the deconvolution procedure leads to a considerable deblurring of the image. In this case, in the deconvoluted image certain residua of the emissivity contrast are visible, which are weak horizontal and vertical dark lines. They point to the fact that the absorptance of the black film was not 100%. In this case, however, this residual emissivity contrast is not dominating, as it was in Fig. 1 (c). Hence it does not disturb here and may be even helpful to orientate on the surface of the IC.

## 6. Conclusions

It has been shown that spatial deconvolution of microscopic LIT images is possible, even in the presence of strong emissivity contrast, if the 0°/-90° image is used for deconvolution. This kind of representation of LIT results is advantageous, compared to the usual phase image, since it provides a better spatial resolution. Thus, the 0°/-90° image can be used in all cases where until now the phase image has been used, if thermal blurring is degrading the effective spatial resolution. This kind of inherent compensation of the emissivity contrast is easier and more effective than blackening the surface or the usual separate measurement of the emissivity image, since it does not require any extra measurement and provides a perfect emissivity compensation. However, its application is limited to microscopic problems, where the thermal -90° signal is nearly homogeneous across the investigated area.

## 6. Acknowledgement

This work was supported by EU project ENK6-CT-2001-00573 (PORTRAIT). Many thanks to EM Microelectronic-Marin SA (Marin, Switzerland) for providing the sample for Fig. 3.

## REFERENCES

[1] MALDAGUE (X.P.V.). - *Theory and practice of infrared technology for nondestructive testing*. New York, Wiley, 2001.

[2] BREITENSTEIN (O.) and LANGENKAMP (M.). - *Lock-in thermography - basics and use for functional diagnostics of electronic components*. Berlin, Springer, 2003.

[3] BREITENSTEIN (O.). - *Lock-in IR thermography for functional testing of solar cells and electronic devices*. QIRT Journal **1** (2004) 151.

[4] CREPEL (O.), BEAUDOIN (F.), DANTAS DE MORAIS (L.), HALLER (G.), GOUPIL (C.), PERDU (P.), DESPLATS (R.), and LEWIS (D.). - *Backside hot spot detection using liquid crystal microscopy*. Microelectronics Reliability **42** (2002) 1741

[5] KOLODNER (P.) and TYSON (J.A.). - *Microscopic fluorescent imaging of surface temperature profiles with 0.01°C resolution*. Appl. Phys. Lett. **40** (1982) 782.

[6] CARSLAW (H.S.) and JAEGER (J.C.). - *Conduction of heat in solids*. Oxford, Clarendon, 1959.

[7] NORKUS (V.), GERLACH (G.), and HOFFMANN (G.). - *Process technologies for high-resolution infrared detectors based on LiTaO3*. Proc. SPIE **3892** (1999) 233.

[8] GRADHAND (M.) and BREITENSTEIN (O.). - *Preparation of nonconducting infrared-absorbing thin films*. Rev. Sci. Instr. **76** (2005) 053702.

Proc. Vth International Workshop, Advances in Signal Processing for Non Destructive Evaluation of Materials
Québec City (Canada),2-4 Aug. 2005. © X. Maldague ed., É. du CAO (2006), ISBN 2-9809199-0-X

# Dynamic characteristics of water surface irradiated by different lamps by using infrared thermography

by A. Kamoi[1] and Y. Okamoto[2]

*[1]Graduate School of Science and Arts, University of East Asia, 2-1 Ichinomiya Gakuen-cho, Shimonoseki, Japan; [2]Regional Joint Technology Center, Ibaraki National College of Technology, 866 Nakane,Hitachinaka, Japan*

## Abstract

Human being cannot maintain her life in the earth without air and water. Especially, the nature of water has not been evident even now from scientific viewpoint. It has been reported that it is strongly influenced by the shape of cluster of water molecule, which depends upon water's surroundings such as light, sound, magnet, heat, etc. This study clarifies the behaviors on fluctuating radiation temperatures of water surfaces due to irradiations of infrared and ultraviolet rays. Then, this study considers about relation between cluster of water molecule and characteristics of fluctuating radiation temperature of water surface.

**Keywords :** infrared thermography, radiation temperature, fluctuation, water surface, power spectral density

## 1. Introduction

As mentioned in the abstract, some characteristics of water was investigated by using infrared thermography. It can be recognized that behavior of water depends upon its surroundings such as atmospheric temperature, sound, light, vibration and so on. Even now, these effect against water have not been cleared. Therefore, the authors tried to find the effect due to its characteristics caused by behavior of fluctuating radiation temperature of water surface irradiated by different lamps. Speaking of water we have used different kinds of water like having mineral or radioactive component and that which is artificially treated like electrically deposited or irradiated by light , sound , and so on. In these application fields to drink water in order to maintain life, we have not understood how to drink what kind of water is efficiently healthy to us. Therefore, this study is to try to make clear the water characteristics affected by radiation temperature fluctuation by using the technique of frequency analysis.[1], [2]. This research tries to clarify the water reaction due to irradiation of infrared and ultra violet rays by measuring the radiation temperature distribution on the water surface.

## 2. Experimental Apparatus

### 2.1 View of Experimental Apparatus

Experimental Apparatus was consisted of the below units as shown in Fig. 1.

1) heater units
2) water basin to be tested
3) shutter and cover: Shutter plate made of Al is installed at the space between lamp and water vessel to give the step irradiation to the water surface
4) infrared thermography
5) oscillographic recorder

The above units are explained in the next 2.2.

Figure 1 experimental set up

## 2.2 Main Composition of Experimental Apparatus

### 2.2.1 water Material to be Measured

1) Public Water (civic water)
2) Pyramid Water: it was manufactured by the Great Pyramid Model* to apply the pyramid effect** depending on shape and direction as shown in Fig. 2.
3) Atomic Water: it was manufactured by immersion in the water with radioisotope

*material: acrylic plate of 2mm thickness, size: each base length;920mm, oblique side: 880mm height: 588mm, inclination angle: 51 , each direction of square base length oriented to east, west, south, north, water vessel is set to the location of mass center of pyramid model

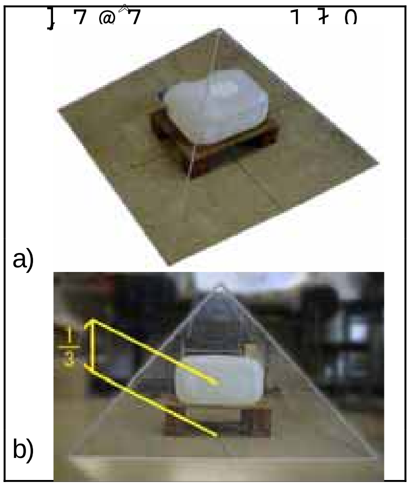

Figure 2 Pyramid model

### 2.2.2 Irradiators

**(1) Infrared Ray Lamp**

1) Heater housing was made of SUS (2mm thickness) and heat sink made of Al was installed at the top of heater for effective natural cooling as shown in Fig.3 a).
2) Heater has 6 infrared ray tubes in which power of each tube is 800 [W], and the total power can be adjusted by switching circuit as. shown in Fig.3 b).

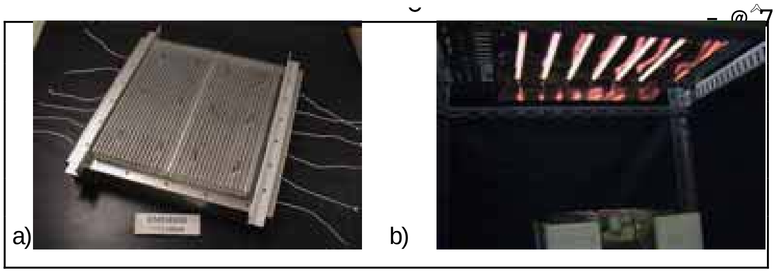

Figure 3 Irradiator for infrared ray: a) outside view b) inside view

**(2) Ultra Violet Ray Lamp**

1) UV Irradiator was composed of 6 UV lamps with stabilizer and lighting system installed on the Al housing as shown in Fig.4 a).
2) Each lamp has power of 10 [W] and radiates middle type of wavelength. The total power can be adjusted by 2 ways of 40 and 60 [W].The small lamps were installed between heater and switch box to operation as shown in Fig. 4 b).

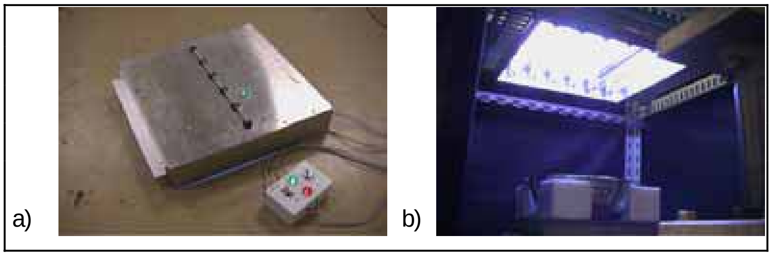

Figure 4 Irradiator for ultra violet ray: a) outside view b) inside view

### 2.2.3 Infrared Thermography

1) type: TH3102 made by NEC Sanei as shown in Fig. 5.
2) infrared sensor: made of HgCdTe, far infrared of 8~13 [ m]
3) thermograms are saved in the inner HDD of control unit of infrared camera
4) radiation temperature related to the thermograms is to be sent to the worksheet of Excel and then treated analytically.

Figure 5 Infrared camera

## 3. Experimental Procedure

### 3.1 Acquisition of Thermograms and Its Condition

1) Water of 3000 cc to be tested is supplied in the vessel made of stainless-steel
2) It is irradiated by IR (infrared ray) and UV (ultra violet ray)

3) The former case is 30s irradiation and 150s natural cooling
4) The latter case is 60s irradiation and 120s natural cooling
5) Thermograms of above two cases were measured by Infrared Thermography

### 3.2 Analysis of Thermograms

1) The cross cursor line in the thermograms is tranformed into radiation temperature distribution after transmitting to Excel by using the software in the off-line of measurement as shown in Fig. 6 a).
2) This fluctuating radiation temperature distribution is analyzed as mean, max., min. and root mean square (that is standard deviation) values in Excel.
3) Then, the mean radiation temperature and its fluctuation distributions on the longitudinal direction of cross cursor line are determined like Fig. 6 b).

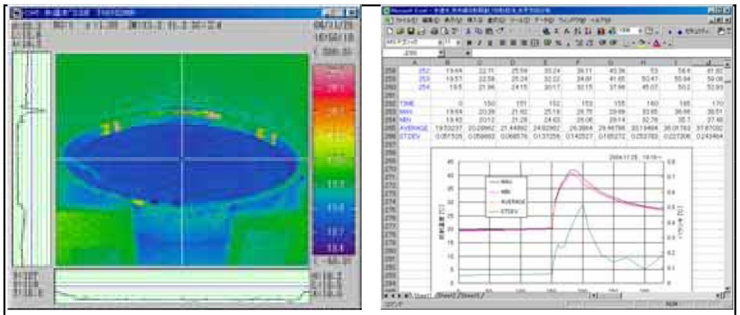

a) thermograms and its analysis b) transportation of radiation temperature to Excel sheet

Figure 6 Procedure of getting the radiation temperature and its fluctuation profiles

### 3.3 Analysis of Power Spectral Density (PSD)

1) The slope of PSD ("n" defined by the equation of PSD = $Kf^{-n}$) becomes "n=1" in case of naturally moderate phenomena such as wind velocity, streaming sound, twinkling star light, etc.. This case is so called by 1/f theory that was discovered by Dr. Musha [3].
2) Recently It has become recognized that fluctuation level becomes larger if n>1 by the authors [2], [4].
3) The center of water surface measured by time trace mode (during 3s per 3ms) is analyzed as power spectral density (PSD) by use of the data analysis software called DADiSP. Then, the slope of PSD is determined by the below equation (1)~(3).

$$\log_{10}PSD = \log_{10}K - n \log_{10}f \qquad (1)$$

$$\log_{10}(PSD_1 / PSD_2) = \log_{10}(f_2 / f_1)^n \qquad (2)$$

$$n = \log_{10}(PSD_1 / PSD_2) / \log_{10}(f_2 / f_1) \qquad (3)$$

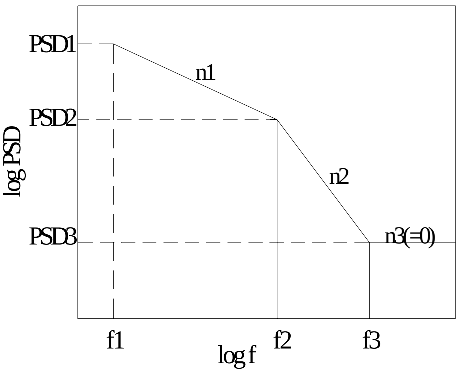

Figure 7 Determination of slope $n_1$, $n_2$, $n_3$ (=0)

## 4. Experimental Results and Consideration

### 4.1 IR Radiation Temperature and Its Fluctuation

The results of radiation temperature distribution and its fluctuation profiles are shown in Fig. 8 a) ~ c).
1) The profile of radiation temperature distribution is almost same in three kinds of waters.
2) But that of each fluctuation distribution shows quite different pattern. The cases of a), c) have max. value after 20s from stopping irradiation and the case b) has two peaks around stopping irradiation.
3) In the cooling process after stopping irradiation, fluctuation pattern shows different behavior.

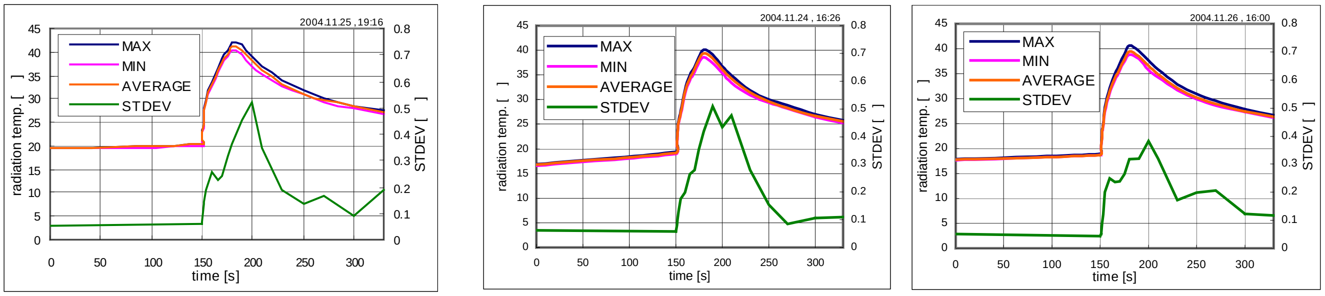

a) public water b) atomic water c) pyramid water

Figure 8 Radiation temperature distribution and its fluctuation

## 4.2 UV Radiation Temperature and its fluctuation

The results of radiation temperature distribution and its fluctuation profiles are shown in Fig. 9 a) ~ c).

1) The profile of radiation temperature is also almost same in three kinds of waters and temperature change is small compared to the case of IR irradiation.

2) Its fluctuation profile shows quite different profile in three kinds of waters.

3) The case a) shows only up and down after UV irradiation, but the cases b) and c) shows peculiar pattern ( it is considered due to shape of the cluster of water molecular).

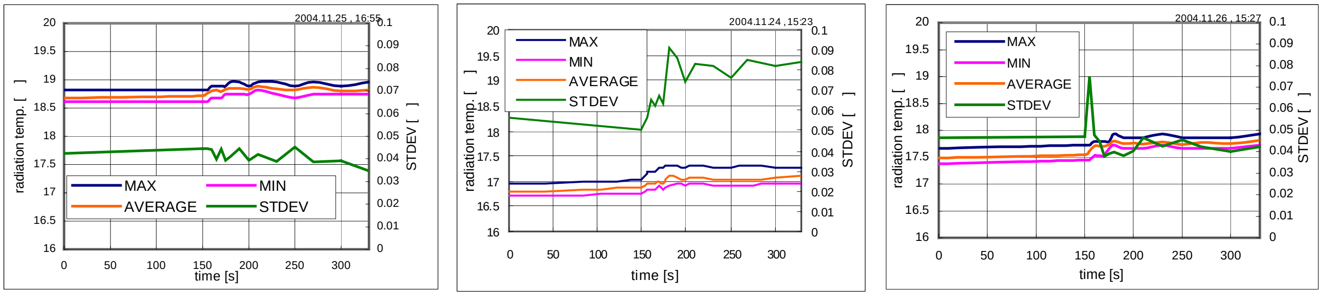

a) pu water b) atomic water c) pyramid water

Figure 9 Radiation temperature distribution and its fluctuation

## 4.3 PSD Graph of IR Irradiation

The PSD graph of IR irradiation are shown as Power Spectral Density (PSD) versus frequency (f) in the case of public water and also in the case of pyramid water in Fig. 10 and Fig. 11, respectively. The slope of PSD was approximately calculated in a low frequency region of f < 0.02 [Hz]. It becomes to be flat like white noise in the region of f 0.05 [Hz].

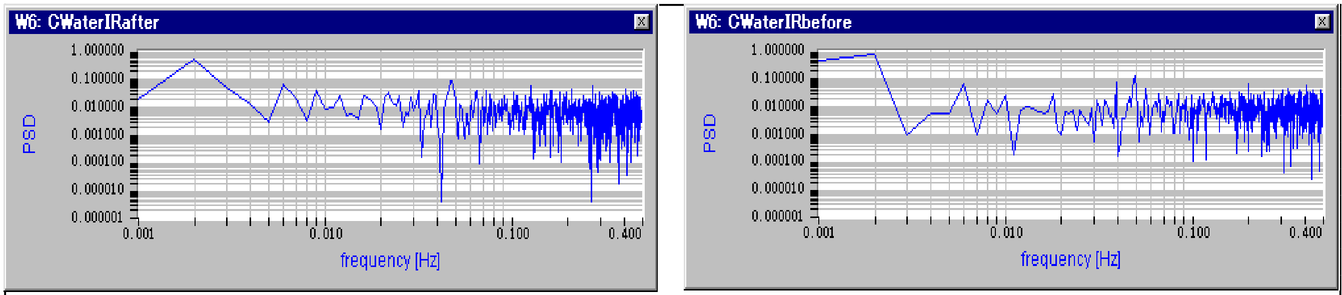

a) before IR irradiation b) after IR irradiation

Figure 10 PSD graph of IR irradiation (public water)

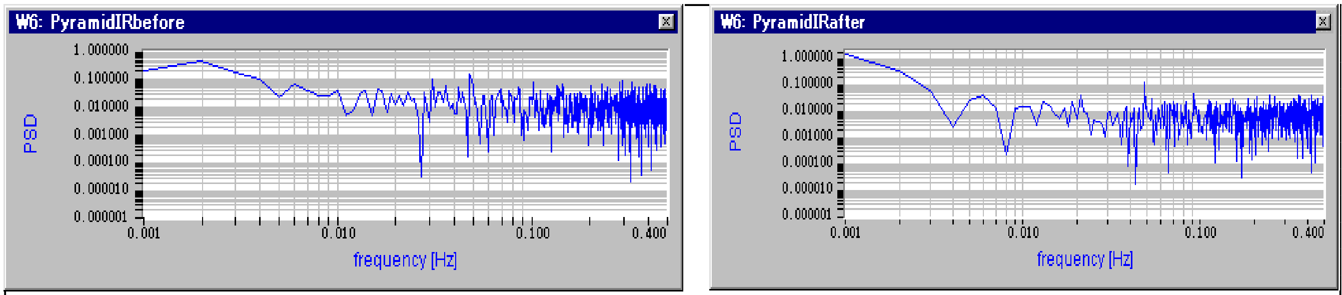

a) before IR irradiation
b) after IR irradiation

Figure 11 PSD graph of IR irradiation (pyramid water)

### 4.4 PSD Graph of UV Irradiation

The PSD graph of UV irradiation are shown as Power Spectral Density (PSD) versus frequency (f) in the case of public water and also in the case of pyramid water in Fig. 12 and Fig. 13, respectively..

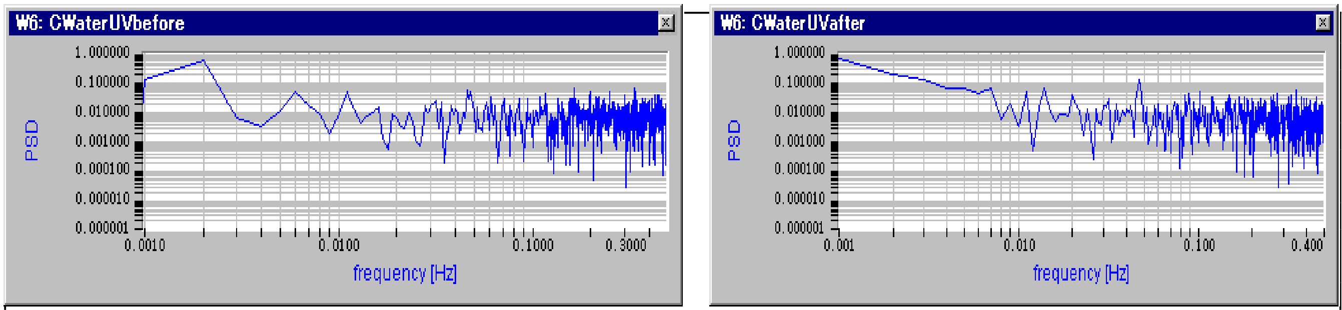

a) before UV irradiation
b) after UV irradiation

Figure 12 PSD graph of UV Irradiation (public water)

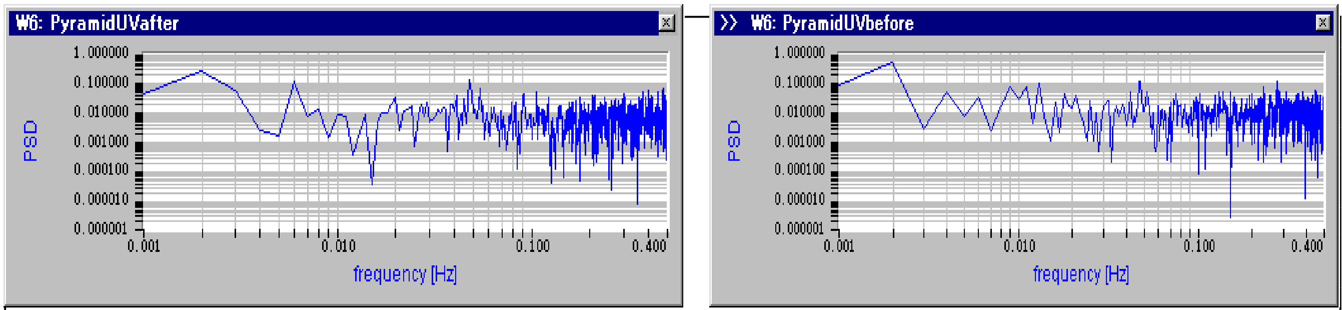

a) before UV irradiation
b) after UV irradiation

Figure 13 PSD graph of UV Irradiation (pyramid water)

### 4.5 Consideration of PSD Slope

1) According to the results by calculating the slope in PSD graphs as shown in Fig.10 to Fig.13, each slope of PSD is shown in Fig. 14 a) and b).
2) It is recognized that each slope of PSD shows different behavior depending upon water type where 1, 2 and 3 is corresponding to public, atomic, and pyramid water, respectively.
3) The slope n in both IR and UV irradiations becomes n>1 and ranged from 1.2 to 2.3. Except the pyramid water, n after irradiation is smaller than n before irradiation.
4) In the case of IR irradiation, pyramid water shows particular behavior that n after irradiation is larger than that

before irradiation.

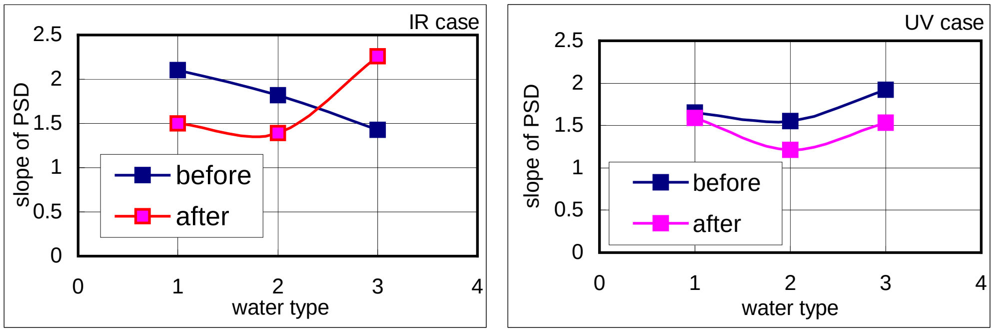

a) IR irradiation b) UV irradiation

Figure 14 Comparison of PSD slope

.

## 5. Conclusion

1) The radiation temperature of water surface became increased by IR irradiation, and gradually decreased after stopping of irradiation. On the contrary it became gradually and slightly increased in the case of UV irradiation.
2) The STDEV of fluctuating radiation temperature in IR irradiation showed approximately same in each water and had max. value at 20 ~ 30s later after stopping irradiation. But that in UV irradiation showed quite particular shape depending on water type. This behavior is considered to be depending on shape of cluster related to motion of water molecule.
3) According to applying the PSD analysis of fluctuating radiation temperature at the only center of water surface, it was clarified that PSD slope is n >1, and n after irradiation is smaller than that before irradiation except the pyramid water.
4) The PSD slope n of the pyramid water showed max. value of 2.26 among three kinds of water, and now its reason was not cleared. Hereinafter, the systematic approach will be expected in this field.

## REFERENCES

[1] Kamoi (A.)and Okamoto (Y.), - *Experimental Study on the Effect of Environmental Fluctuations Affecting the Thermal Images of Infrared Radiometer*, Proceedings. of SPIE, Vol. 4020, 2000, p. 374

[2] Kamoi (A.) and Okamoto (Y.), - *Study on Variation of Thermal Image by Infrared Radiometer Influenced by Fluctuations of Environmental Factors,* Journal of Visualization, Vol. 5, No. 1, 2002, p. 95

[3], Musha (T.),- *1/f Fluctuation Appeared in Living Body*, Nature, Vol. 11, 1979, p. 60

[4] Agu (M.), Teramachi (Y.), Yamanaka (K.) and Sumiya (M.), - *Some aspects on Application of Fluctuating Phenomena, Applied Physics*, Vol.61, No.7, 1992, p. 690

Proc. Vth International Workshop, Advances in Signal Processing for Non Destructive Evaluation of Materials
Québec City (Canada),2-4 Aug. 2005. © X. Maldague ed., É. du CAO (2006), ISBN 2-9809199-0-X

# Development of a NDT method using thermography for composite material inspection on aircraft using military thermal imager

By : P. Servais[1] and N. Gerlach[2]

[1] *Competence Center Flying Material, Non Destructive Testing Squadron, 1130 Brussel, Belgium*
[2] *University of Liege, Rennequin Sualem School, Aerospace engineering Department, 4000 Liège, Belgium*

## Abstract

*This paper describes the methodology used to introduce thermography as new inspection method for composite parts in aircraft maintenance. It is here focused on two main topics : control of leading edge flaps of Belgian F16 (mainly due to ageing aircraft) and inspection of main and tail rotor blades of Belgian A109 Agusta helicopters. The new idea is to use typical military thermal imagers initially bought for surveillance which only give grey level images but with a good thermal sensitivity and spatial resolution and to develop a specific signal processing of digitized images.*

**Keywords** *: thermography, aircraft maintenance, NDT, composite inspection, thermal imager, military imager*

## 1. Introduction

TNDT (Thermal Non Destructive Testing) is now an emerging method that comes out of laboratory since a few years. It is here proposed to investigate, compare and quantify the different possibilities to use thermography instead of radiography or ultrasonic testing on composite parts in maintenance of military aircrafts. The new idea is to use military thermal imagers also used by the infantry (see figure 1) because the detector is now an infrared focal plane array capable of measuring a very faint difference of temperature (less than 0.07 K)

Figure 1 : military Thermal imager used by Belgian Defense

Thermography is particularly adapted for non destructive testing on composite and can be used on different materials:
- carbon-epoxy
- thin metal skin on honeycomb structure (like aircraft doors)
- epoxy resin with glass fibre reinforcement GFRP
- panel skins with CFRP (Carbon Fibre Reinforced Plastic) like helicopter blades

The control contributes to highlight the most prominent types of discontinuities seen in aerospace composites including [1]

- porosity which reduces the compressive load carrying capability,
- water ingress or moisture which can degrade the mechanical properties of some resins or lead to freeze inside the part causing more and more damage (see picture 2 for honeycomb composite part with central view of hotter area in the centre of the piece viewed in white in picture 2)
- disbond or delamination resulting from low strength in the resin
- impact damage during the taxi or caused by bird strike or by a dropped tool during maintenance
- inclusions which can reduce strength by kinking the fibres around the inserted material

Some defects like water ingress cause high thermal difference on the surface as seen on Fig 2 below. This thermal difference depends on their characteristics, their dimensions and their depth in the piece part. So the camera should have good thermal resolution (NETD or Noise Equivalent Temperature Difference). [2] Recent work made by Italian Air Force showed that 0.1 ml water ingress in one cell of honeycomb flap of AMX aircraft could show a thermal difference of 1°C when surface is heated with a flow of 15000 W/m$^2$.[3]

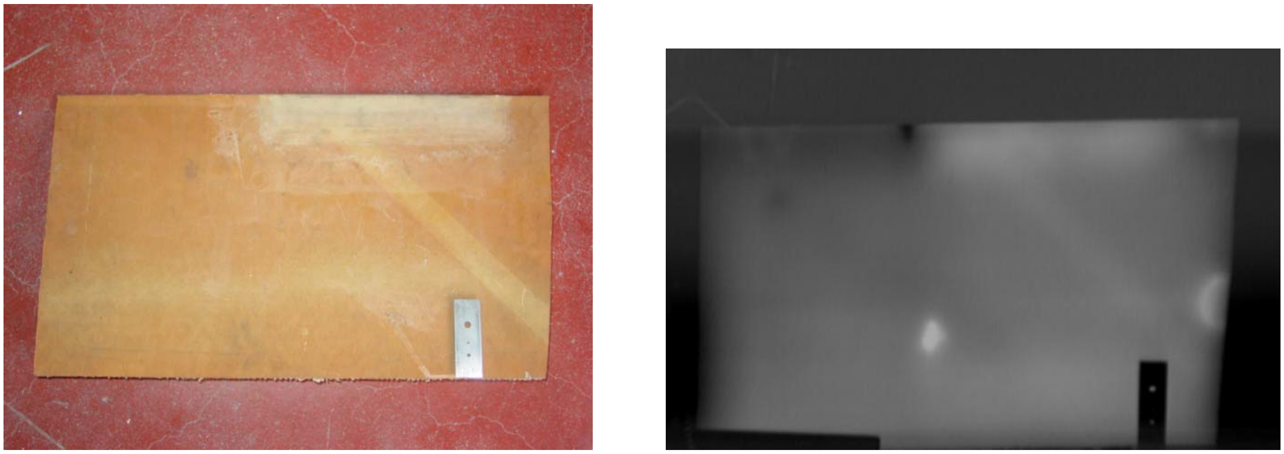

Figure 2 Left : composite part with hole type IQI, Right : thermal image of composite part with water ingress

## 2. Application to F-16 leading edge and Agusta main and tail rotor blades

The inspection of composite materials is an increasingly important topic due to the expanding number of uses to which such materials are being put. Due to its lightness, composite is used in large quantities in aeronautical applications. For example, F-16 leading edge and Agusta rotor blade are exclusively built in composite.

Composite materials can be affected by manufacturing processes defects (voids due to volatile resin components, foreign bodies, ply cracking, delaminations, bonding defects...) and by in-service defects (fracture of fibres, cracks, delaminations, ingress of moisture, inclusions, impact damage,...).

In case of F-16 leading edge and Agusta rotor blade, it is challenge of outstanding importance to detect defects as precisely as possible. This should avoid unnecessary scraping of expensive material and increase serviceability of parts.

Until now, only tap testing is used to verify integrity of F-16 or Agusta composite parts, mainly because radiography can not detect delamination and because ultrasonic is a point to point technique not practical for parts as long as blades with a length of 5 meters . This test delivers only approximate information on the wellbeing of the material.

It is thus important to develop a more reliable non destructive testing methodology especially adapted to composite materials.

Thermography is an incoming non destructive testing tool that presents some key advantages in comparison with the other available technologies, namely:

- It is totally non-contacting and non-invasive.
- It can inspect relatively large areas in a single snapshot.
- The data are pictorial format, which is always amenable for the formation of rapid decisions.
- The data are easily stored and retrieved with any classical laptop.
- It allows fast inspection rates (on line information).
- The security of personnel is guaranteed when compared to radiography.

Furthermore, there is no real difficulty to obtain adequate equipment (IR camera, thermal stimulation units, frame grabbers, laptop) as this material is widely used in the Defence. This should reduce drastically the cost of the application and facilitate a large diffusion of this NDT technology amongst all Defence organizations as for example on fig 3 with our military training Alphajet.

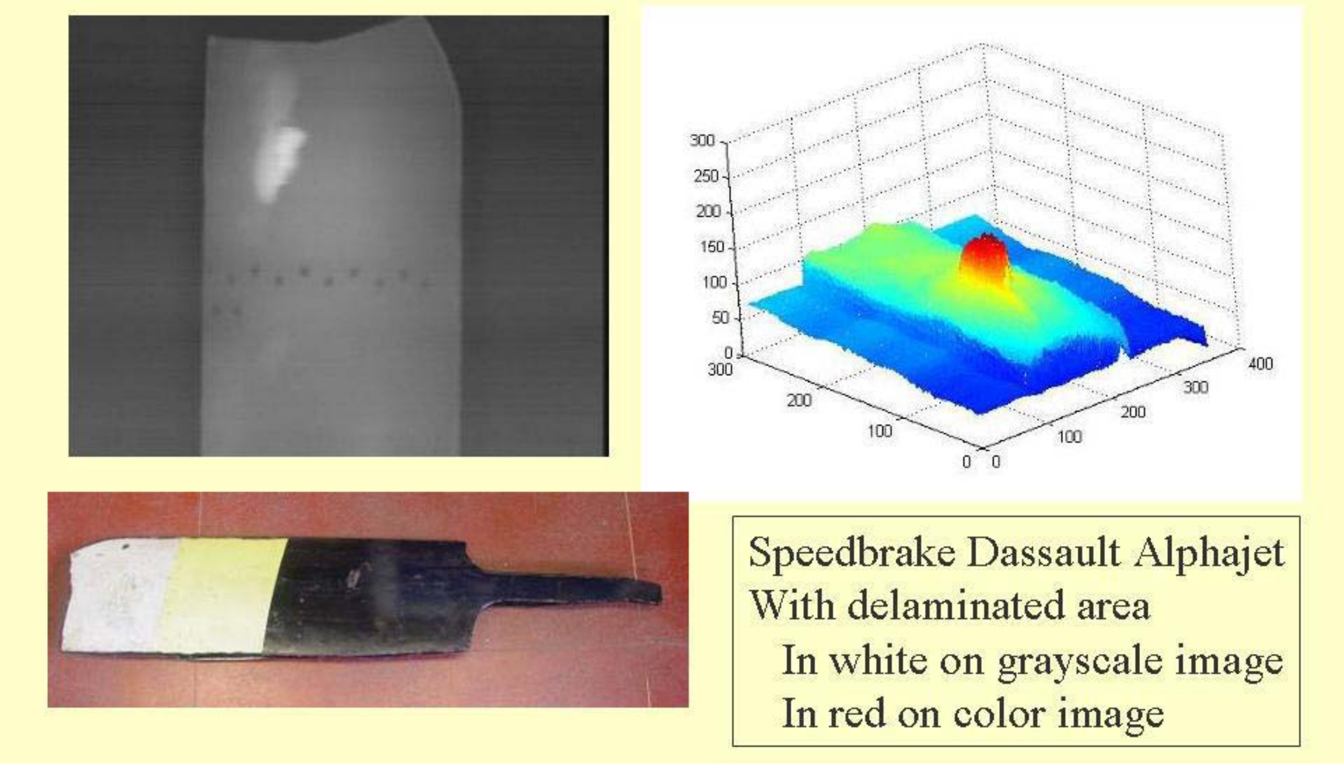

Speedbrake Dassault Alphajet
With delaminated area
In white on grayscale image
In red on color image

Figure 3 : Example of use of our military thermal imager to detect delamination on Belgian training Aircraft

## 3. Choice of heating procedures

3.1 A first approach will compare the most popular heating procedures like :

- optical heating (flash tubes, projector, tubular halogen lamps, UV light) ,
- air flux heating (air dryer, thermal paint remover, portable electrical heater 2700 W,…)
- specific heating blankets used also for composite repair

The comparison will take into account main heating properties: repeatability, uniformity, timeliness, duration. The thermal imager can easily be used to retrieve these characteristics but a real laboratory camera can also be used to quantify temperatures directly and more easily.

3.2 A second approach will be an experimental study of raw images obtained using several heaters.

For each method, determination of the more adequate parameters to be used in order to optimise defect detection in a raw image of a known sample:

- final temperature obtained
- duration of the heating (flash or long pulse)
- location and orientation of the heater, start up time to be at constant temperature

## 4. IR detectors

4.1 A Theoretical comparison between the available detectors will take into account different characteristics of the thermal detector:

We compare our military imager from Thalès with a classical civilian IR camera FLIR SC3000

- Type of IR detector : our military thermal system uses a FPA (Focal Plane Array) HgCdTe hybridized on a silicon CMOS readout circuit
- Type of cooler (our photovoltaic detector is cooled by miniature Stirling-cycle rotary cooler)
- Noise equivalent temperature difference, here less than 0.07 K obtained at the military air conditioned laboratory with calibrated blackbody (with a precise regulation at 0.01°C)

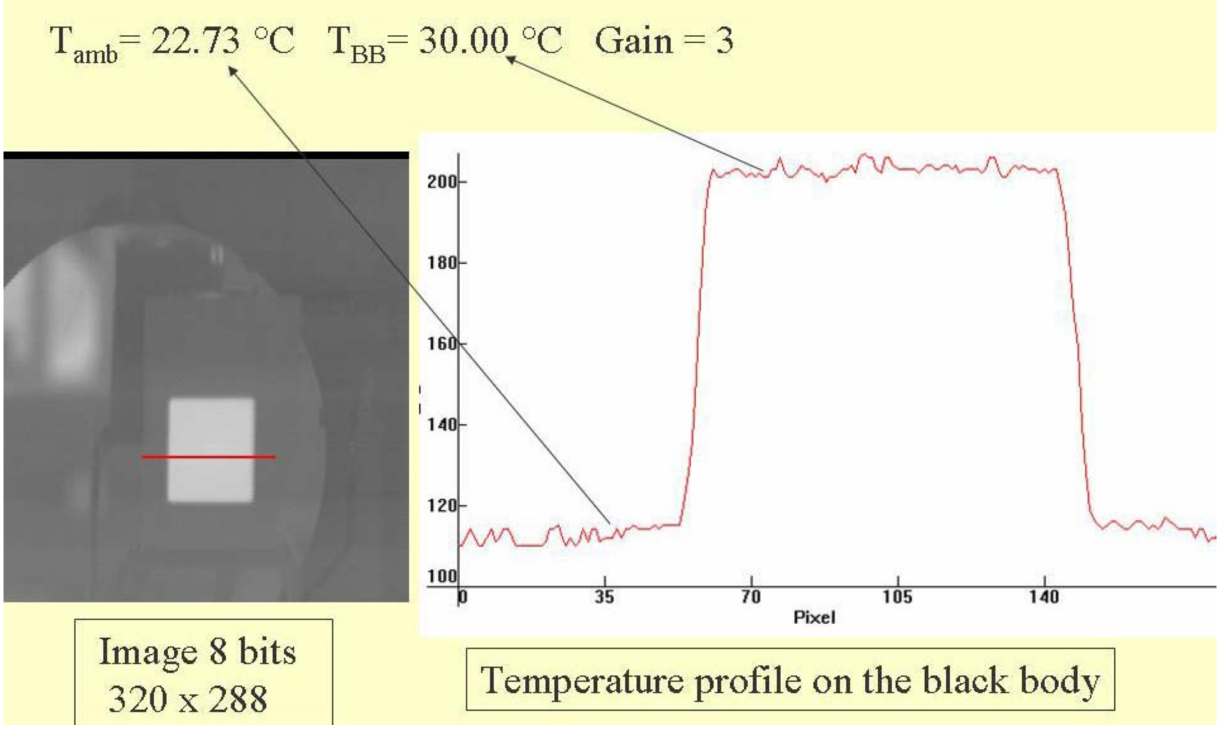

Figure 4. Thermal image made on our calibrated blackbody and temperature profile (graylevel units)

- Detectivity D* (sensitivity figure of merit of an infrared detector) > 2.3 $10^{11}$ Jones for our camera.
- Minimum resolvable temperature difference (the smallest temperature difference that an operator can clearly distinguish out of the noise) checked with calibrated blackbody at the laboratory with different observers following ASTM E 1213 [4].
- slit response function (spatial resolution) also compared during other tests with hole type IQI placed on part to have a reference spatial information at lower temperature than the part [5]
- Selection of the proper atmospheric band (short wave IR 3-5 µm for FLIR or longer wave 8-12 µm for our military thermal imager)

4.2 An experimental comparison of raw images obtained with different detectors obtained with different cameras will permit to use a calibrated test sample containing different types of defects, of different sizes and at different depths.

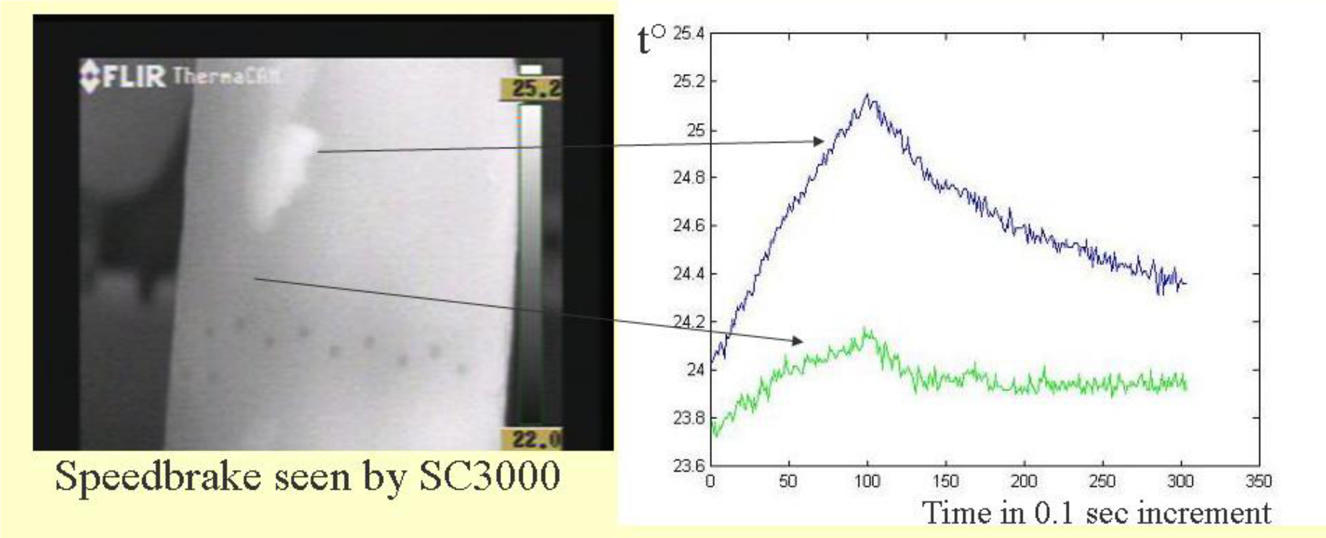

Figure 5 : Alphajet speedbrake tested with FLIR camera with T° evolution during 30 sec on 2 relevant points

## 5. Choice of a thermography technique

To get a portable inspection method it is here first experienced with pulse thermography. This inspection relies on a short thermal stimulation pulse, with duration of a few seconds for low conductivity specimens (such as graphite epoxy laminates). Such thermal stimulation allows direct deployment with convenient heating sources and prevents damage to the component. The pulse thermography consists of briefly heating the part to inspect and then recording the temperature decay curve. The temperature of the material changes rapidly after the initial thermal pulse because the thermal front propagates by diffusion, under the surface and also because of radiation and convection losses. The presence of defect reduces the diffusion rate so that when observing the surface temperature, defects appear as areas of different temperatures with respect to surrounding sound area once the thermal front has reached them. Consequently, deeper defects will be observed later and with a reduced contrast.

## 6. Signal processing :

After the choice of the technique and the calibrated sample, it is necessary to realize signal processing of the thermal acquisition, mainly because of :

(1) Noise consideration :
  - Experimental determination of noise from the IR detector, electronic noise, noise from external source, noise caused by object inhomogeneity.
  - Reduction of noise by adding lots of thermograms.

(2) Camera calibration : vignetting effect, temperature computations (calibration curve).

(3) Choice of best contrast computation : absolute contrast, running contrast, normalized contrast, standard contrast or differential absolute contrast.

(4) Processing and experiment for non-planar surface inspection (like a composite cone with honeycomb of an aircraft like our Belgian C130)

(5) Image processed in false color view to increase seeability by NDT technician

## 7. Experimental results on known samples

After having processed the acquisition, it must be evaluate some important features of the new technique like :

(1) Reduction in image contrast with defect depth

(2) Effect of host material thermal properties

(3) Temperature decay at the surface over a defect at different depths

(4) Thermal contrast produced at the surface by defects at different depths.

(5) Peak magnitude of the temperature contrast evolution depending of the defect depth

(6) Thermal signature of different defects: delamination, disband and water ingress

## 8. Validation of the NDT technique

As always in NDT, the new technique must be validated statistically by use of POD (Probability Of Detection) and compare with radiography and ultrasonic C-Scan of the parts. The idea is to characterize the defect detected with 90% of POD following the methodology defined in Working Group AVT051[6].

## 9. Application of the NDT technique

The whole fleet of Belgian F-16 and Agusta helicopters must be inspected with the technique in order to detect defects and to characterize them.

## 10. Edition of a NDT technique user guide, course and certification scheme

For the NDT technicians of the industry, it is important to establish a reference training Handbook for level 1, 2 and 3 and to certify people into thermography. The used samples and the rejected flying parts are collected for training and examination at the certification centre of the Belgian National Aerospace NDT Board to be able to certify people following NAS410 or EN4179 which does not for the moment recognize thermography but it has to be done in the near future.

---

**REFERENCES**

[1] Nondestructive Testing Handbook, Third Edition, Vol 3 Infrared and Thermal Testing, Chap 15, ASNT, 2001, p495-496

[2] ASTM E 1543, Test Method for Noise Equivalent Temperature Difference of Thermal Imaging System, 1994

[3] RTO-MP-AVT-124, Water detection in Honeycomb structures by use of Thermography, RTO Publication, 2005, p28-3

[4] ASTM E 1213, Standard Test Method for Minimum Resolvable Temperature Difference for Thermal Imaging System, 1997

[5] Nondestructive Testing Handbook, Third Edition, Vol 3 Infrared and Thermal Testing, Chap 20, ASNT, 2001, p 695

[6] The Use of Field Inspection Data in the Performance Measurement of Nondestructive Inspections
Final Report of the Applied Vehicle Technology Working Group 051, RTO publication

Proc. Vth International Workshop, Advances in Signal Processing for Non Destructive Evaluation of Materials
Québec City (Canada),2-4 Aug. 2005. © X. Maldague ed., É. du CAO (2006), ISBN 2-9809199-0-X

# Characterization of delamination by a thermal method of non destructive testing

**A. Obbadi, S. Belattar**

*Laboratory of Energetic and Processing of the Signal Faculty of Sciences, 24000 El Jadida, Morocco*

## Abstract

Thermal non destructive testing (TNDT) is a technique for obtaining surface temperature profiles on a structure, and subsequently relating this information to some imperfections within the structure. The tests of TNDT are generally based on the observation and the exploitation of a thermal phenomenon disrupted by the presence of an anomaly or heterogeneity. Indeed, an anomaly or a flaw inside the structure will generally alter the heat flow through the structure due to the difference in its heat transfer properties and those of the unflawed structure. If the heat flow pattern is sufficiently altered, a difference of temperature in the structure in the unflawed and the flawed regions is observed. The methods of analysis of these phenomena are based on the codes of numeric modeling using the method of the finite elements by help of commercial software. The simulations realized take into account the position and the thickness of the delamination and its thermophysical characteristics.

**Keywords:** Finite elements, delamination, heat transfer, thermal NDT (TNDT).

## 1. Introduction

The processes of heat transfer seem to pervade all aspects of our life. These processes that occur, for example, in engineering equipment, in the heating and air conditioning of building, play a vital role that can be observed in a great variety of practical situations. Composite materials [1,2] are of increasing interest to the industry and their performance characteristics are desirable. Often, an internal anomaly within these structures modifies strongly their physical properties. Thermal non-destructive testing is able to reveal the presence of a defect without damaging the specimen [1]. It employs heated surface temperature variations caused by delamination [1-5], cracks, voids, corroded regions…etc. In all these cases, predictions offer economic benefits because no experimental study can be expected to measure the distributions of all variables over the entire domain. For this reason, even when an experiment is performed, there is great value in obtaining a companion computer solution to supplement the experimental information. Among the different methods of predictions [6,7], the numerical solution based on finite element method [8] seems quite promising. Numerical analysis is useful to consider different defect geometry and determine their detectability without the expense of making and testing the corresponding specimens. Will to improve quality and safety of materials, many techniques of non destructive testing (NDT), adapted to these new materials and the specific defects that they can present were born. Among them, the methods known as thermal [1-8], have the advantage of allowing a fast inspection and with or without contact. In this great family, the thermal control method is characterized by its simplicity of implementation and its relative insensitivity to the surrounding noises. It thus is particularly adapted to an industrial use.

## 2. Position of problem

The goal of this part is to calculate the thermal response of a delaminated wall [1-5] subjected to a uniform continuous and extended step function of flow Q on the input surface. The back face being maintained at a constant temperature Ta = 25°C, the others faces are insulated. It is supposed that the excitation is applied in a uniform way to considered surface. In order to simplify calculations, we limit ourselves to the case of a circular delamination in an isotropic material. The problem then has rotation symmetry around axis z (FIG. 1); it is thus possible to limit the study to 2D in which only a half-section of the object is represented (FIG. 2). Delamination is located at the depth $l_1$ and has a diameter d and a thickness e. The thickness of the back face of the sample is noted l2 and the simulated length is equal to 50 times $l_1$ in order to minimize the edge effects. The method of characterization use commercial software, based on the finite element method [9]. It permits, at any moment, to calculate the evolution of temperature and in any point of material supposed isotropic.

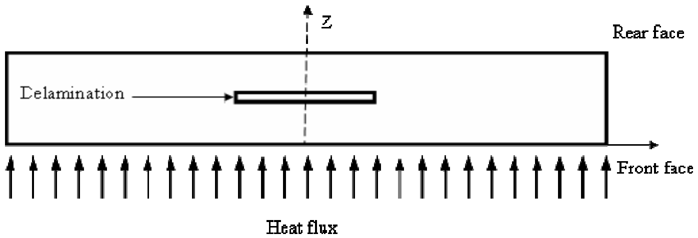

Figure 1: Geometry representation: complete wall

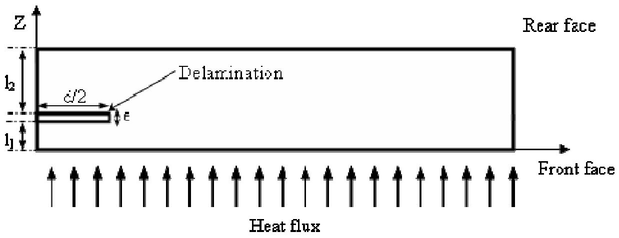

Figure 2: Geometry representation: half-section

### 3. Theoretical study

The equation of diffusion of heat is written, in cylindrical coordinates and supposing that thermal conductivity is constant, one obtains:

$$\frac{\rho C}{k}\frac{\partial T}{\partial t}=\frac{1}{r}\left[\frac{\partial}{\partial r}\left(r\frac{\partial T}{\partial r}\right)\right]+\frac{\partial^2 T}{\partial z^2} \tag{1}$$

Where: ρ represents the density of material, C its massive heat capacity, and K its conductivity thermal. We consider the depth $l_1$ of the defect as the characteristic length. The dimensionless variables marked of asterisk are:

$$r*=\frac{r}{l_1},\ z*=\frac{z}{l_1},\ e*=\frac{e}{l_1},\ d*=\frac{d}{l_1},\ l*=\frac{l_2}{l_1},\ t*=\frac{at}{l_1^2},\ \text{and}\ T*=\frac{T}{T_a} \tag{2}$$

Where: t* is the Fourier number attached to $l_1$, *a=k/(ρ.c)* is the diffusivity of material, and Ta ambient temperature. In the space of the dimensionless magnitudes. The relation (1) becomes:

$$\frac{\rho * C *}{k *}\frac{\partial T *}{\partial t *}=\frac{1}{r *}\left[\frac{\partial}{\partial r *}\left(r *\frac{\partial T *}{\partial r *}\right)\right]+\frac{\partial^2 T *}{\partial z *^2} \tag{3}$$

With the proviso of posing: $\rho * = 1,\quad C* = 1,\quad et\quad k* = 1$ (4)

### 4. Resolution of the equations

### The mesh description

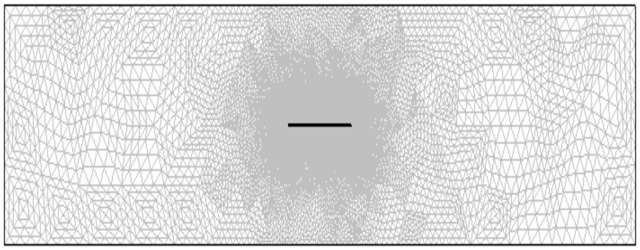

Figure 3: mesh representation of the complete wall with defect

In a cylindrical reference mark, only a "half-section" of the sample requires a mesh. In order to emphasize the mesh density around the defect the whole wall presented (FIG. 3). The defect is simply simulated by an absence of matter. Its thickness is constant and equal to $l_1/100$. Taking into account the symmetry of the problem, study is limited to two dimensions one in a cylindrical.

## 5. Results of simulations

To illustrate the previous theoretical considerations, we present the computation results of the thermal response in the case of an isotropic material, the considered concrete is characterized by K = 1,7W/m.k (thermal conductivity) ρ = 2250 kg/m3 (density) and C = 827J/kg.k (specific heat). The delamination is characterized by K = 0,0272 w/m.k (thermal conductivity) ρ = 1,057 kg/m3 (density) and C = 717,8 J/kg.k (specific heat), d* = 1, and l* = 1. After resolution of the posed problem, it is possible to plot the distribution in temperature on the totality or a part of the wall at a given moment, as well as the temporal evolution of the temperature in a given point (FIG. 5). In the presence of the defect the heat flow has tendency to propagate avoiding the defect as shown it figure 5. This phenomenon conducts to the rise in the temperature at the location of defect, represented by a thermal patches figure 5. The maximum of this temperature gives an estimate on the required resolution of the equipment of non destructive testing. At the exit of the defect the lines of flow tend to be standardized. This could be information in the form and the position of the defect in material. Figure 6 shows the variation in the temperature along the entry surface (front face). In general a temperature higher than the average at the entry reveals the presence of a resistive defect in the structure. The agreement between these results and those already obtained by using a code of finished volumes [6,7], make it possible to validate this thermal calculation.

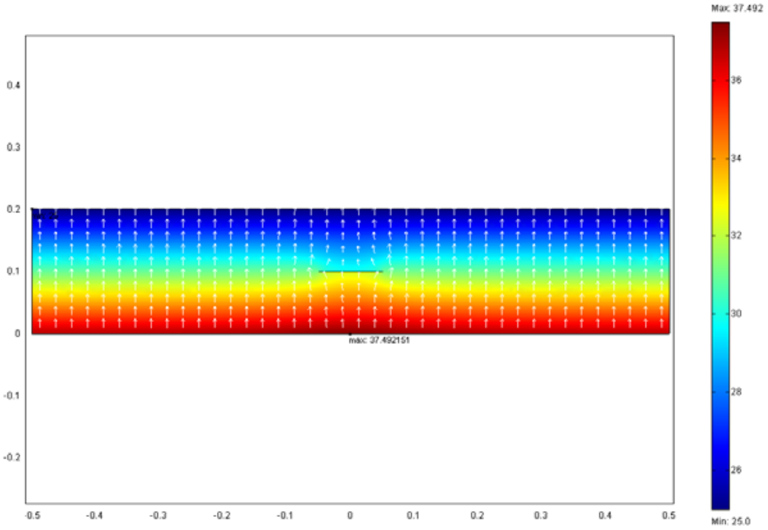

*Figure 5: Temperature distribution of the complete wall (Arrow: Heat flux, Surface: Temperature)(d*=1 - l*=1 - e*=0,01 - Q=100w)*

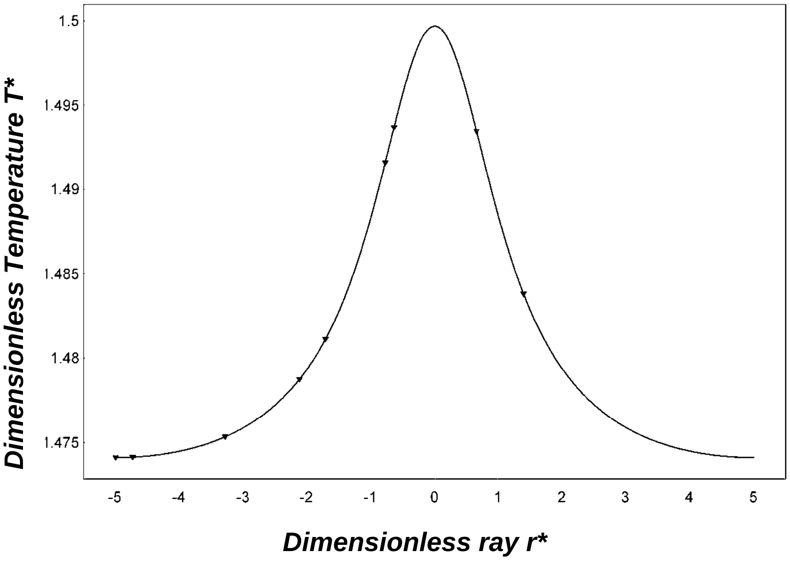

*Figure 6: temperature profile on the entry surface (d*=1 - l*=1 - e*=0,01 - Q=100w)*

### 5.1. Study of the influence of the defect parameters

The paramount parameters studied in this work are: defect diameter, defect position, defect thickness, and material, containing defect, nature.

#### 5.1.1. Influence of defect dimensionless diameter

The curves of FIG. 7 represent the surface temperature for four values, of diameter d*, varying from 0.5 to 0,8 with the following progression: 0,5 - 0,6 - 0,7 and 0,8. At the location of defect deformation increases with the value of the dimensionless diameter.

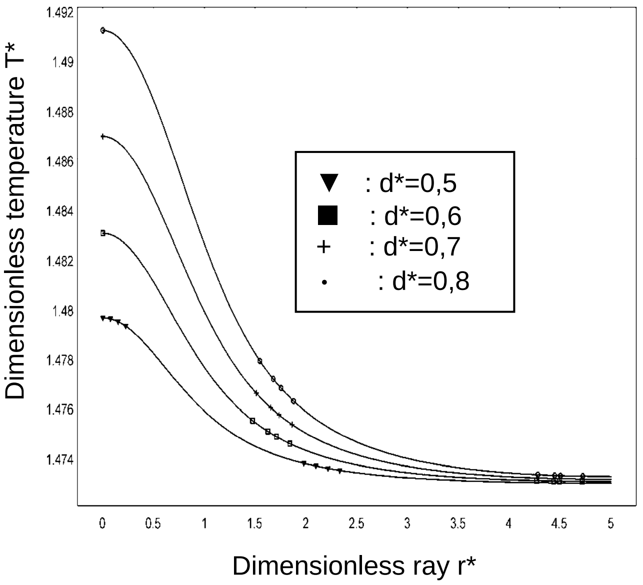

*Figure 7: Influence of defect dimensionless diameter on the entry surface temperature profile (l*=1 - e*=0,01 - Q=100w)*

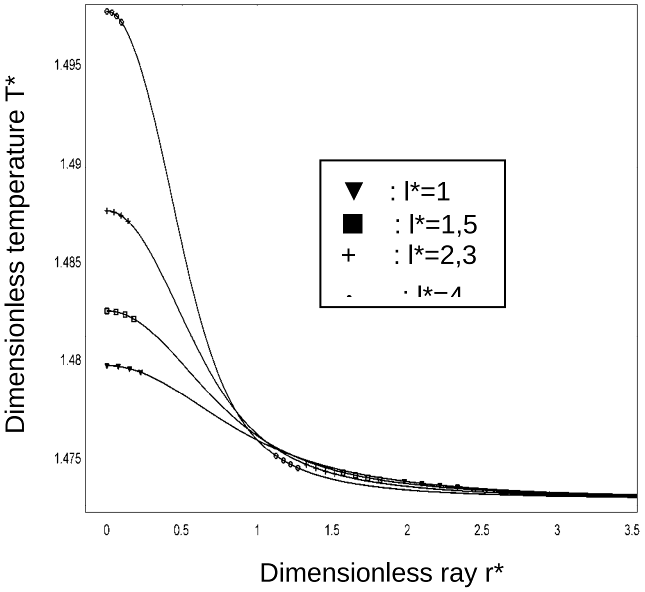

*Figure 8: Influence of defect dimensionless position on the entry surface temperature profile (d*=1 – Q=100w)*

### 5.1.2. Influence of the defect dimensionless position

To study the influence of the defect position, the response of the sample containing a defect (delamination) whose diameter dimensionless is d* = 1, is calculated. The defect position l* varying from 1 (defect with mid thickness) to 4 (defect close to the surface of entry). From the curves evolution according to r* (FIG. 8), one realizes that curves tend towards a limit as one approaches the case of a surface defect (l* = 4). This case, of course unfavorable for the NDT, constitutes the lower limit of detectability of the defects. The deformation at location of defect increases with the value of the dimensionless position. On the other hand, one can notice that the evolution form of these profiles is different from that obtained previously (FIG. 7).

### 5.1.3. Influence of defect dimensionless thickness

The curve, figure 9, represents the evolution of the surface temperature according to the dimensionless ray r*, for four different thicknesses of defect in the structure. The thickness e* takes the following values (0,01; 0,03; 0,06; and 0,09), and for each thickness the defect was placed at the position l*=1. The temperature profiles, show that the dimensionless temperature T* passes by a maximum, in the case of the resistive defect (figure 9). This maximum represents the point on the entry surface on the center of defect where it is more effective or optimal to make control, because it is the point to which the maximum in temperature difference T* for detection occurs. While moving away from the defect the surface profile tends towards a constant value (figure 9). The curves figure 9 show that the profile of temperature T* is strongly related to the thickness of the defect. A great value of T* would result from a great thickness of defect (figure 9). In this case, the defect presence detection would be simple, with the help of adapted equipment, and in the contrary case, it is necessary to have very sensitive equipment.

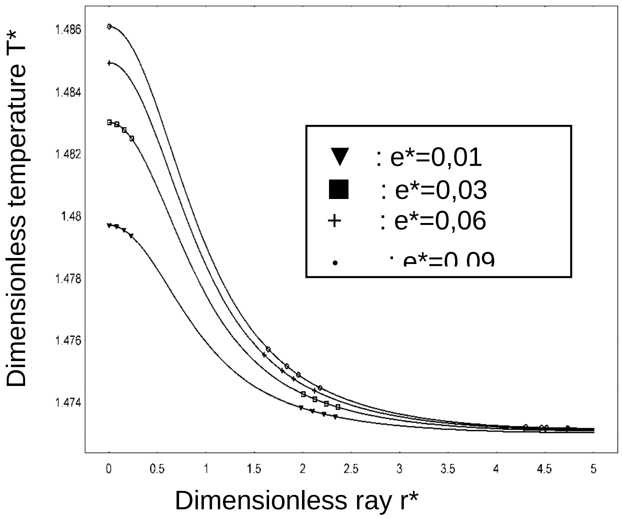

*Figure 9: Influence of defect dimensionless thickness on the entry surface temperature profile (d*=1 – Q=100w)*

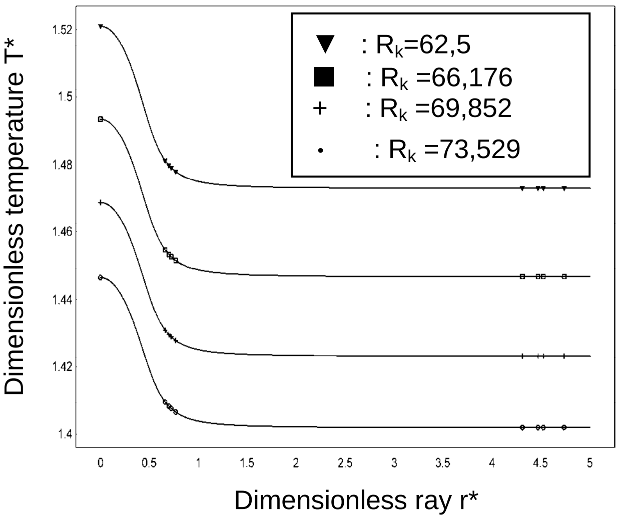

*Figure 10: Influence of the material, containing the defect, nature on the surface temperature profile (l*=0,11 - e*=0,05 - d*=5 – Q=100w)*

### 5.2. Influence of the material, containing defect, nature

The physical nature of material containing defect influences enormously on the difference in temperature T* as figure 10 shows it. It is a configuration where the wall takes four values of conductivities report/ratio $Rk=K_{material}/k_{Delamination}$ (Rk =62,5 (Concrete), 66,176 (Grinding door), 69,852 (other) and 73,852 (Marble) w/m.k). The defect is characterized by: l*=0,11, d*=5 and e*=0,05. The results represented by figure 10 shows that a strong conductivity of the defect compared to that of the structure which contains it, brings a deficit of temperature of surface to the structure entry, and a low value of conductivity will involve an excess of temperature. For our model a zero value of (T* material – T* delamination) is representative of the thermal homogeneity of material.

### 5.3. Influence of the excitation intensity

Whatever the thermal NDT method active or passive used and the type of equipment (thermocouple, radiometer, scanner, infra-red camera) the goal is to facilitate the location and to allow a control of the thermal anomalies. It is necessary to correctly choose the source of energy in the case of the active method and the time of measure in the case of the passive one. The curves, figure 11, represent the evolution of the surface temperature T* according to the dimensionless ray r*, for defect thickness e*=0,01 and four values of the heat flow (Q=100, 100,5, 101 and 101,5w). The defect position l* is taken equal to 1 in a wall of 500mm of thickness. A great value of T* would result from a great value of the flow of excitation as shows it the results represented by figure 11. In this case, the defect presence detection would be simple, with the help

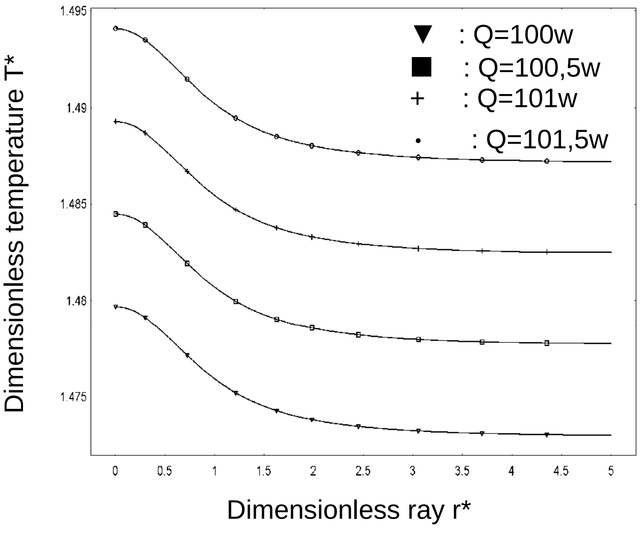

*Figure 11: Influence intensity of the excitation on the profile of surface of entry (l*=1 - e*=0,01 - d*=1)*

of adapted equipment, and in the contrary case, it is necessary to have very sensitive equipment.

## 6. Conclusion

In this work, we studied the case of a material containing a circular delamination subjected to a thermal excitation. We set out to analyse the influence of the defect parameters on the measurable magnitude, we showed that it is theoretically possible to detect any defect, with the proviso of applying a sufficient energy and to have an important contrast in conductivities material defect, it is different in practice. Indeed, this model relates to a resistive defect in a rigorously plane plate. However, if one introduces a light initial curve (what is practically the case in reality), one realizes that the thermal gradient exiting between the heated face and the back face is at the origin of a total deformation of the plate which can completely occult the deformation at the location of the defect. This phenomenon, which is very often observed at the time of measurements, makes that it very difficult to detect the defects whose dimensionless diameter is very low. All calculations were carried out in the case of an isotropic material, but the taking into account of the anisotropy would be possible with the proviso of using a computer code which allows it.

## REFERENCES

[1] AVDELIDIS (N.P.), ALMOND (D.P.), DOBBINSON (A.), HAWTIN (B.C.), IBARRA-CASTANEDO (C.) and MALDAGUE (X.). - Aircraft composites assessment by means of transient thermal NDT. Progress in Aerospace Sciences 40, Elsevier science, 2004, p. 143–162.

[2]GUILLAUMAT (L.), BATSALE (J.C.) and MOURAND (D.). - Real time infra-red image processing for the detection of delamination in composite plates. Composites Part A: applied science and manufacturing 35, Elsevier science, 2004, p. 939–944.

[3] SAKAGAMI (T.) and KUBO (S.). - Development of a new non-destructive testing technique for quantitative evaluations of delamination defects in concrete structures based on phase delay measurement using lock-in thermography. Infrared Physics & Technology 43, Elsevier science, 2002, p. 311–316.

[4] VARIS (J.), RANTALA (J.) and HARTIKAINEN (J.). - An infrared line scanning technique for detecting delaminations in carbon fibre tubes. NDT&E International, Elsevier Science, Vol. 29, No. 6, 1996, p. 371-377.

[5] COUTELLIER (D.), WALRICK (J.C.) and GEOFFROY (P.). - Presentation of a methodology for delamination detection within laminated structures. Composites Science and Technology, Elsevier science, 9p. 2005.

[6] OBBADI (A.), BELATTAR (S.), BEIHAQI (M.), TMIRI (A.) and BALLOUTI (A.). - Two-dimensional Analysis of Thermal non Destructive Evaluation, by the numerical method of control volumes. IV International workshop- Advances in signal processing for Nondestructive Evaluation of Materials, X.P.V. Maldague, Technical Editor ASNT Volume 6, Canada, August 2001, p. 195-200.

[7] OBBADI (A.), BELATTAR (S.), SAHNOUN (S.) and TMIRI (A.). - Analyse numérique des profils de température et de flux: application au contrôle non destructif. Journal PCN (Physical & Chemical News) volume2, Numéro2, 2001, p. 49-53.

[8]OBBADI (A.) and BELATTAR (S.). - Méthode des éléments finis appliquée au contrôle thermique non destructif (CTND) tridimensionnel en génie civil. Revue marocaine du génie civil 1er trimestre, volume1, N°105, 2004, p.16-21.

Proc. Vth International Workshop, Advances in Signal Processing for Non Destructive Evaluation of Materials
Québec City (Canada),2-4 Aug. 2005. © X. Maldague ed., É. du CAO (2006), ISBN 2-9809199-0-X

# Software Tool in *Java* for Infrared Image Processing: *TermUV*

**H. Benitez, H. Loaiza,E. Caicedo, B. Bacca, H. Jimenez, M. Barreto, J. Vargas**

*Research Group Perception and Intelligent Systems, Universidad del Valle, Colombia,*
*e-mail: hloaiza@univalle.edu.co*

## Abstract

This paper presents the design, implementation and results of a thermal image processing tool, which allows the capture, pre–processing and processing of thermal images through a graphical script interface, then, generate reports and store results in a data base. Each stage (capture, pre-process, process and reports) was designed and implemented keeping in mind modularity, flexibility and portability criteria.

**Key Words: Thermal Image Processing, Thermography, Thermal inspection, Software Architecture, Graphical Programming.**

## 1.Introduction

Currenlty, there is an increasing necessity for standardization in thermal images processing for inspection and maintenance. The methods currently used are becoming more complex and their integration is necessary in order to achieve a more efficient inspection. Several tools that integrate these methods have been developed for commercial or academic purposes. The commercial tools, such as *Display IMG, TeamSoftware, Irmotion, Goratech Ireport*, etc, are generally linked to a specific type of infrared camera and allow the capture, storage, report generation, analysis and processing of images. Moreover, some of these tools allow the processing in real time.

On the other hand, academic tools have also been created in order to promote the use of infrared TNDT (Thermal Non Destructive Testing) from the laboratory in the industrial environment [1]. In addition, they are used to solve three dimensional heat conduction problems of heating a layered solid that contains several subsurface defects [2].

Both commercial and academic tools can be used in several platforms (Windows 98 / Windows 2000/Windows NT/Windows XP version ) and they do not include algorithms for the use of AI (Artificial Intelligence) methods. On the other hand, they do not provide the user with the opportunity of adding new processing modules to the existing ones, and they do not offer especial profiles for users depending on their level of expertise.

The subject of this article is to present the structure and the application of *TermUV (Térmico Universidad del Valle),* a flexible and modular software tool for the analysis of infrared images. It was implemented in *JAVA* and some functions are based on *ImageJ* [3] (open source code for image processing ) permitting the addition of preprocessing, processing and AI modules devoted to the TNDT (Thermal Nondestructive Testing) field. Moreover, it allows graphical programming.

The first section of this article describes the software system design and image processing tools. Then, it presents several results of its application. Finally, it describes directions for further development of the tool.

## 2. Software Architecture

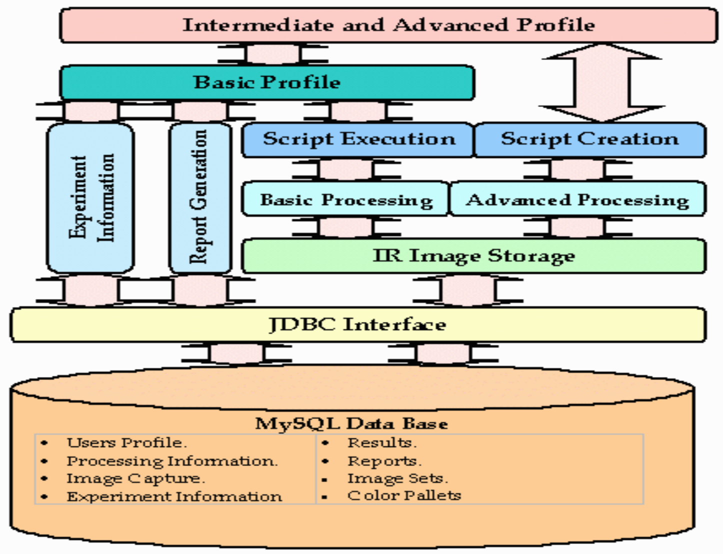

Figure 1
Software structure

The figure shows the software structure implemented in *TermUV*. This is explained in a top – bottom fashion:

- There are three user profiles: Basic, Intermediate and Advanced, which are implemented as a Wizard in order to help to develop all the application stages.
- Regardless of user profile, tools like: Experiment Information, Report Generation and Script Execution are available. Nevertheless, the Script Creation tool is only available for advanced users, in such a way that more processing and analysis tools can be used such as: Wavelet Transformation, Pattern Recognition using Neural Networks and special processing tools used in thermography.
- Intermediate and Advanced users can use the Image Storage Tool in order to save results obtained in middle stages meanwhile a Script is created.
- The whole of these tools are supported on a JDBC interface, which instantiates Image Sets, Processing and Experiment Information, Reports, Results and Project objects taking into account the information stored on a data base.
- Finally, in our case we use a MySQL data base to save the whole project information about each user profile.

Other important software structure characteristics are:

- The Image Processing Tool is supported on the *ImageJ* package.
- The Script Execution and Creation Tools are supported on the *ImageAPP* package, allowing the execution and creation of scripts using a graphical approach.
- The Artificial Neural Networks tool for data processing is based on the well-known *Joone* package

### 2.1 General Image Processing

The tool provides a set of useful algorithms for general-purpose image processing in addition to those provided specifically to support thermography. These algorithms include image acquisition, image arithmetic, image enhancement, pseudocolor display and image examination.
Several images with different sizes and formats can be manipulated with *TermUV*. The formats supported are: GIF, JPEG, BMP and TIFF. Images can be converted to 8, 16 and 32 bits.

### 2.1.1 Image Mathematics and Logic

The image mathematic and logic commands provide pixel-by-pixel operations on one or more images. The commands *Sumar, Restar, Multiplicar* and *Dividir* take the corresponding arithmetic operations (Addition, Subtraction, Multiplication and Division) and store the result in another image. Moreover, the logical operations allowed are NOT, AND, OR and XOR.

### 2.1.2 Image Enhancement

The image enhancement commands provide the design of several standard convolution and frequency filters to emphasize or smooth selected features of an image and facilitate interpretation by the user.
The size and parameters of convolution filters masks can be specified by the user allowing the creation of a wide range of filters that can be used to eliminate noise or emphasize image details.
On the other hand, it is possible to design a bandpass filter that filters out large structures (shading correction) and small structures (smoothing) of the specified size by Gaussian filtering in Fourier space. It is also possible to apply the Sobel edge detector in order to highlight sharp changes in intensity in the image. Furthermore, the tool is able to remove smooth continuous background from images and to modify the bright and contrast of the image in order to facilitate its interpretation. In addition, the command *Surface* plays a three-dimensional graph of pixel intensities in a grayscale or pseudo color image. On the other hand, the algorithms *Correccion de Vignetting* and *Remocion de pixels* allows the correction of vignetting effect [4] and the removal of bad pixels presented in thermographic images, respectively.

### 2.1.3 Pseudocolor display

The use of pseudocolor is an image enhancement that increases contrast or color codes an image to correspond to temperature or gray level. The tool can create a reversed image, similar to a photographic negative, of the entire image or selection. Similarly, it is able to apply the LTU (Lookup table) *Fire* to the image in order to assign color to image grey values.

### 2.1.4 Image Analysis

The image examination commands provide quantitative information about the image. For this purpose the *TermUV* has these algorithms: *Detección de defectos, Histograma, ROI* and *Profiler*. Moreover, it allows image feature extraction such as: mean, standard deviation and seven invariant moments [5] that can be used to train a neural network specified by the user. Similarly, the FFT (Fast Fourier Transform) and 2D DWT (Discrete Wavelet Transform) can be obtained from the image.
The command *Deteccion de Defectos* is able to automatically detect defects. This algorithm is based on the fact that TNDT images have a limited number of spatial frequencies [6]. The first step is to localize the defect and then specific thresholds are found in the image to estimate the border of the defects. Each threshold is found by means of a region growing approach [7], which starts at the central point of a defect and stops when either an image border is hit or the number of pixels agglomerated

together around the seed (central point) increases abruptly. On the other hand, the command *Histograma* computes image histogram, mean, standard deviation, maximum and minimum grey level values of the image. In addition, the ROI (Region of Interest) command permits working with oval and round area selections to compute the histogram in these areas and extracts their statistical parameters. Likewise, the *Profiler* command displays a two dimensional graph of the intensities of pixels along a line within an image.

## 3. Results and Discussion

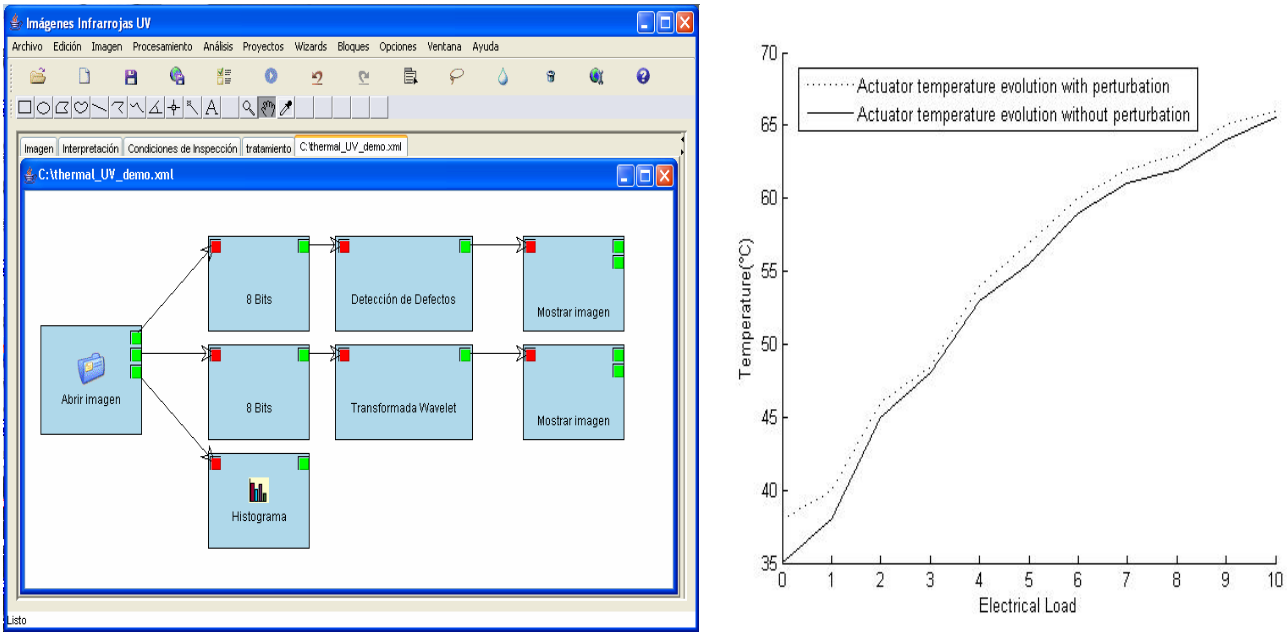

(a) (b)

Figure 2

(a)Graphical programming structure for actuator unit thermogram analysis (b) Actuator Temperature Evolution

The sample graphical program in Figure 2a shows the use of several blocks implemented in *TermUV* applied for thermogram analysis using the graphical script interface. This thermogram represents the function of an actuator unit and was obtained with the IR camera Thermovision A20 whose thermal sensibility is 0.12°C at 30°C. For this experiment the distance between the camera and the target is 0.7 m and the electrical current consumed by the actuator is 1.7 A when a mechanical perturbation is applied to the actuator. Figure 2b describes the actuator temperature evolution with perturbation and without perturbation. The absolute actuator temperature at which the thermogram was taken is 63 °C.

The first block is used to open the image file, this file may have extensions bmp**,** tiff or jpg. The following blocks, *8 bits* and *Histograma*, are used to change the image to an 8 bits image and then calculates the image histogram, respectively. From this point, two algorithms are applied for the thermogram analysis. The first one is used for defect automatic detection and the other one is used to calculate the thermogram Wavelet transform.

On the other hand, the 2D DWT is applied for one level of decomposition, and for horizontal, diagonal and vertical details. The objective of this test is to highlight image details and detect hot spots produced either by friction or excessive electrical load.

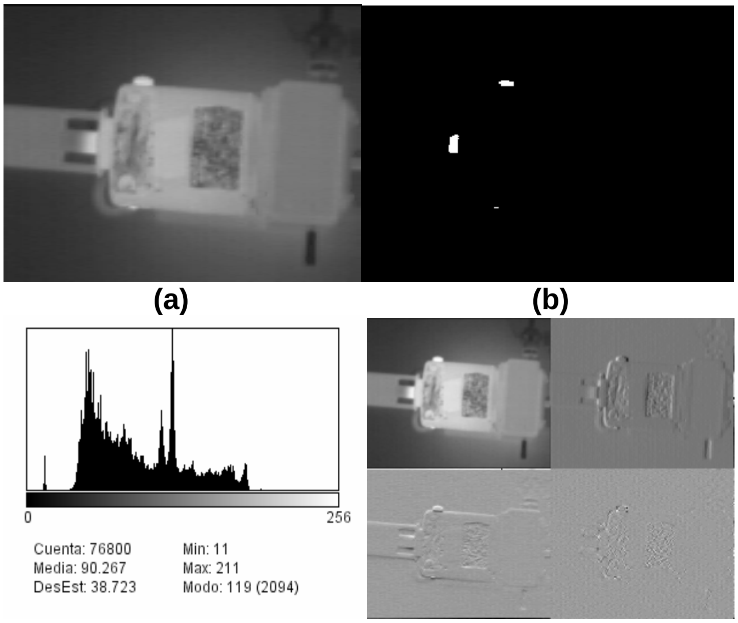

**(a)** **(b)**

**(c)** **(d)**

Figure 3
Results after applying the graphical programming structure of Figure 2a

Figure 3 shows the results of applying the image processing graph presented in Figure 2, figure 3a is the thermal image to be processed and figure 3b is the defect map produced by the automatic defect detection algorithm. The algorithm detected three *hot spots* in the actuator, which has an overheating between the shaft and the actuator body due to friction.

For this case the input parameters were: 3 for the maximum number of defects that can be found in the image and 10 for the MND (Maximum Neighbourhood Distance). On the other hand, figure 3c is the histogram and provides statistical image parameters such as: mean, standard deviation, Mode, Max and Min of the statistical grey level distribution. Figure 3d represents the application of 2D DWT with Haar basis function and one level of decomposition showing horizontal, vertical and diagonal details. Furthermore, *TermUV* is able to apply other Wavelet basis functions such as: *Daubechies* up to 9th order and *Biorthogonal* with different orders of decomposition and reconstruction.

## 4. Conclusions and future developments

*TermUV* is at its initial development stage and our group is working on testing and inclusions of new algorithms that implement new procedures that are currently arising from the prolific TNDT field such as: Differential Absolute Contrast (DAC) [8] and thermal PCA (Principal Component Analysis) [9].

The need for fast processing makes *ImageJ* more appropriate for this application than *JAI (Java Advanced Imaging)* since the former is able to work directly with the pixels while *JAI* creates a new data type and operates the pixels with this data type.

On the other hand, only the algorithms devoted for the beginner user will be available for the public domain given the copyright category of some algorithms implemented.

*TermUV* allows the integration of the principal methods using in NDT and is useful as an educational tool for academia as well as a practical tool aiding in the everyday tasks of inspection in the field. Finally, *TermUV* might encourage the development of experimental platforms at lower prices and make arise the research interest about TNDT in Colombia and other Latin-American countries.

## 5. Acknowledgements

Special acknowledgement for financial support is extended to COLCIENCIAS and Universidad del Valle. Also, the authors want to thank the help provided by Mr X Maldague and Mr C Ibarra at Université Laval.

## REFERENCES

[1] VAVILOV V ET AL - *Inversion of experimental data and thermal tomography using "Termo.Heat" and "Termidge" software*. Proceedings QIRT 94.

[2] VAVILOV V - *Thermofit Pro$^{TM}$ Operation Manual* , 2004.

[3] http://rsb.info.nih.gov/ij/docs/index.html Last access: 28-07-2005.

[4] MARINETTI ET AL 95 – *Calibration Procedure for Focal Plane Array Cameras and Noise Equivalent Loss for Quantitative Thermographic NDT*, Materials Evaluation 1997.

[5] GONZALEZ R -*Digital Image Processing* - Prentice Hall 793 p 2001

[6] MALDAGUE X ET AL - *Thermographic Nondestructive evaluation: An algorithm for Automatic Defect Extraction in Infrared Images*, IEEE Transactions on Systems, Man and Cybernetics vol 20 No 3 May/June 1990.

[7] MALDAGUE.X - *Theory and Practice of Infrared Technology for Nondestructive Testing* ,Wiley Interscience 683 p.2001.

[8] IBARRA ET AL 04 - *Infrared image processing and data analysis* Infrared Physics and Technology 2004.

[9] MARINETTI - *Statistical analysis of IR thermographic sequences by PCA* Infrared Physics and Technology Volumen 46 Issues 1-2 December 2004.

[10] HUGHETT P– *A programmable command interpreter to automate image processing of infrared thermography* SPIE Vol 1467 Thermosense XIII 1991.

[11] ESTABLE L – *IRNDT : Logiciel intégré de traitement d'images infrarouges en JAVA*- RAPPORT D'ACTIVITIES ANNUAL REPORT 1997-1998,Laboratoire de Vision et Systèmes Numeriques,Université Laval 1998

[12] BENITEZ H ET AL - *Application of Image Processing Algorithms for Image Enhancement and Defect Detection in Infrared Thermography for Nondestructive Testing*, Memorias del IX Simposio de Tratamiento de Señales e Imágenes y Visión Artificial, Manizales, ISBN 958-9322-91-3,2004.

[13] CEBALLOS 00 – *JAVA 2 Curso de programación*, Alfaomega, 2000

Proc. Vth International Workshop, Advances in Signal Processing for Non Destructive Evaluation of Materials
Québec City (Canada),2-4 Aug. 2005. © X. Maldague ed., É. du CAO (2006), ISBN 2-9809199-0-X

# Shape Effect on Blind Frequency for Depth Inversion in Pulsed Thermography

M. Genest[1], E. Grinzato[2], P. Bison[2], S. Marinetti[2]
C. Ibarra-Castanedo[1], X. Maldague[1]
[1] Electrical and Computing Eng. Dept., Université Laval, Quebec City (Quebec) Canada[1]
[2] ITC-CNR, Padova (Venice) Italy[2]

## Abstract

In this paper, a study is presented indicating that the specimen shape, for orientation smaller than about 30°, does not affect the blind frequency obtained in Pulsed Phase Thermography processing. Therefore, it makes this measurement suitable for depth inversion in the case of non-flat shaped specimens. Theory and experimental results are discussed.

## 1. Introduction

Infrared (IR) pulsed thermography (PT) [1] experiences a fast deployment in NonDestructive (NDE) evaluation nowadays. In some instances, the part to be inspected is of complex shape. Little studies have been devoted to those cases, especially if quantitative depth retrieval is of interest (see for instance [2, 3, 4]). In fact it is easily conceived that, with respect to a situation where a specimen is flat, the case of a complex shape - let say a tilted for now – specimen will provide a different temperature measurement if all other parameters are the same. This is due to the local orientation $\theta$ of the surface (Fig. 1, left).

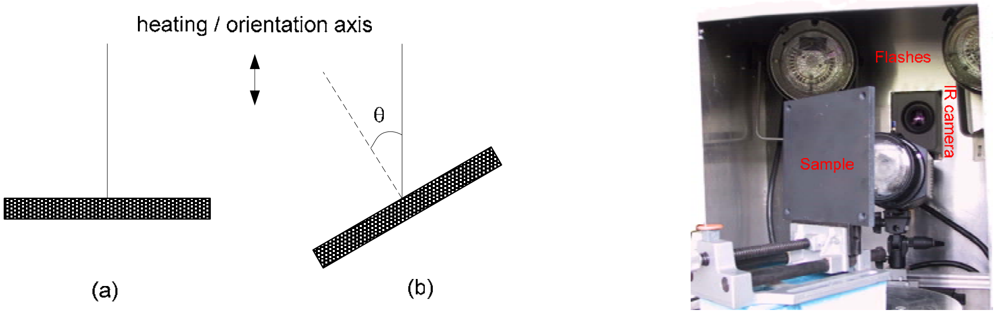

Figure 1 Flat and tilted plate (left), experimental set-up for IR thermography NDE (right).

We recall that in pulsed thermography, the specimen is submitted to a thermal pulse which causes its surface temperature to rise. Assuming a photo-thermal pulse of energy, the specimen surface temperature rises and then decays due to natural cooling (Fig. 1, right). The temperature decay is of interest since thermal waves launched into the specimen by the heating pulse reveal defects at a time which depends on defect depth [1].

---

[1] maldagx@gel.ulaval.ca
[2] ermanno.grinzato@itc.cnr.it, paolo.bison@itc.cnr.it, sergio.marinetti@itc.cnr.it

Pulsed Phase Thermography (PPT) is a signal processing in which the specimen behaviour in PT is analysed not in the time domain but rather in the frequency domain [4]. PPT studies were found particularly helpful if phase is considered. Moreover, recent studies showed that depth inversion can be easily performed by extracting blind frequencies [5]. In this paper, the effect of shape orientation (that is local orientation θ) is considered in regards of depth inversion with blind frequency.

## 2. Theory

### 2.1 On orientation $\theta$

Pulsed heating of a semi-infinite homogeneous specimen (Fig. 1-a, left) causes the surface temperature to rise and then decay. Assuming a simple 1-D case, the temperature decay T can be defined as [1, eq. 9.8]:

$$\mathrm{T} = \frac{\mathrm{Q}}{\mathrm{e}\sqrt{\pi \mathrm{t}}} \tag{1}$$

where Q is the amount of energy absorbed by the specimen, t is the time and e is the thermal effusivity of the specimen defined as $\sqrt{\mathrm{k}\rho\mathrm{C}}$ with k the thermal conductivity, $\rho$ the mass density and C the specific heat.

If we suppose a PPT subsequent processing [5], the temperature decay recorded by the IR camera (Fig. 1, right) will be subject to a discrete Fast Fourier Transform (FFT) so that data is moved from the time domain (discretized here as N data per image pixel along the time axis) to the frequency domain leading to:

$$\mathrm{T(k)} \Leftrightarrow \mathrm{F(n)} \tag{2}$$

$$\mathrm{F} = \sum_{k=0}^{N-1} T(k) e^{2\pi i k n / N} = \mathrm{Re}_n + i\,\mathrm{Im}_n \tag{3}$$

where F is the FFT of T, $i$ is the imaginary number ($\sqrt{-1}$), Re and Im are the real and imaginary parts of the transform, k stands for the time increment and the n designates the frequency increment.

The phase and amplitude images are finally obtained from the known relationships:

$$A_n = \sqrt{\mathrm{Re}_n^2 + \mathrm{Im}_n^2} \text{ and } \phi_n = \arctan\left(\frac{\mathrm{Im}_n}{\mathrm{Re}_n}\right). \tag{4}$$

Now, in the case of a tilted component and assuming a uniform surface heating Q of the surface, we have to consider the surface orientation θ. Angle θ affects the measurement in two ways. First, assuming orthographic heating, only cos θ of the energy contributes to the heating (this comes from the projection in the heating direction). Second for a "lambertian" surface, only cos θ of the subsequent surface heating will be emitted in the direction of the IR camera (this comes from the projection in the observation direction). Hence, the observed tilted surface temperature T' will be reduced by a factor:

$$T' = \cos^2\theta \cdot T \,. \tag{5}$$

Following eq. (3), knowing that the Fourier transform is a linear operator, and since $\cos^2\theta$ is a constant here (it does not depend upon time), we see that:

$$A_n^{'} \approx \sqrt{\cos^2\theta \cdot \mathrm{Re}_n^2 + \cos^2\theta \cdot \mathrm{Im}_n^2} \text{ and } \phi_n^{'} \approx \arctan\left(\frac{\cos^2\theta \cdot \mathrm{Im}_n}{\cos^2\theta \cdot \mathrm{Re}_n}\right). \tag{6}$$

Here "$\approx$" symbol was used since such an analysis is only approximative due to the particular irradiation deployed. Clearly, in PPT, amplitude A images will be affected by surface orientation θ while phase $\phi$ images should not be much since parameter $\cos^2\theta$ cancels out in the division process of eq. (6).

Before terminating this section, the following table shows the value of $\cos^2\theta$ for several orientation θ. It is seen than for orientations of less than about 30° surface orientation should not affect much the data assuming a common level of uncertainty (Table 1).

Table 1. Values of $\cos^2\theta$ as function of $\theta$.

| $\theta$ | $\cos^2\theta$ | $\theta$ | $\cos^2\theta$ |
|---|---|---|---|
| 10° | 0.97 | 40° | 0.59 |
| 20° | 0.88 | 50° | 0.41 |
| 30° | 0.75 | 60° | 0.25 |

### 2.2 On depth inversion with blind frequency $f_b$

In PPT, the blind frequency $f_b$ is the frequency at which the phase value $\phi_d$ of a defect of given depth $z_d$ merges with the phase value of the sound material [7]. It was demonstrated that $f_b$ and $z_d$ can be related using the following relationship for depth inversion [6]:

$$z_d = C_1 \phi_d \sqrt{\frac{\alpha_d}{\pi f_b}} + C_2 \tag{7}$$

Where $C_1$ and $C_2$ are regression coefficients $C_1$ being related to material properties and $\alpha_d$ is the thermal diffusivity ($\alpha_d = k/\rho C$). This equation is directly derived after the thermal diffusion length $\mu_d = (\alpha_d / \pi f_b)^{1/2}$. In fact in [8], author mentions a value of $C_1 \approx 1.8$.

## 3. Experiments

In order to verify the previous discussion, several experiments where conducted on two different specimens, identical in all respect but *Specimen 1* was made of CFRP (Carbon Fiber Reinforced Plastic) while *Specimen 2* was made of GFRP (Glass Fiber Reinforced Plastic). Both samples have the shape of a cylinder with a curvature radius of 27.5 cm and several defects (square Teflon inserts of different sizes: 5 rows of 5 square defects of size: 3, 5, 7, 10, 15 mm and of different depths from 0.2 to 1 mm) located between plies during fabrication. Furthermore, during the experiments, the specimens were tilted with respect to the heating/observation axis (Fig. 1) to get more orientations to analyse (Fig. 2).

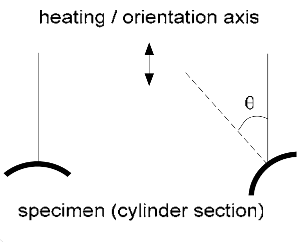

Fig. 2 Specimen tilted with various orientations $\theta$.

The specimen was tested by pulsed thermography (Fig. 1, right). Figure 3 confirms what was said in Section 2 (eq. (6)): phase is relatively insensitive to orientation while amplitude is.

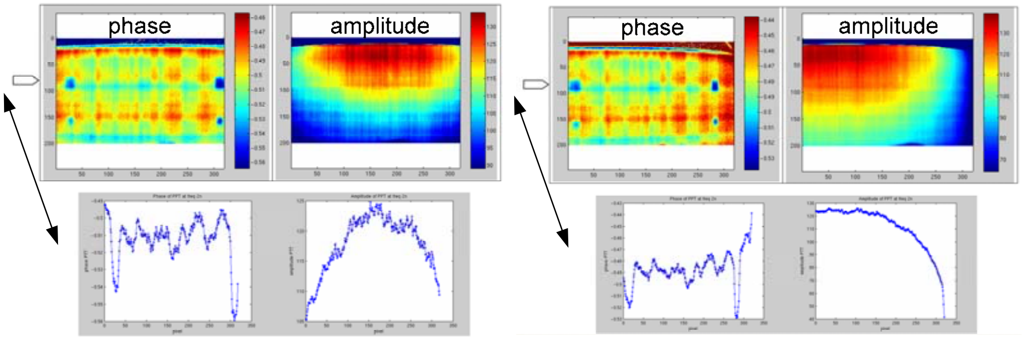

(a) (b)

Fig. 3 Effect of orientation on phase and amplitude for *Specimen* 1 made of CFRP with orientation of (a): 0° and (b): 20°. Second discrete frequency (0.167 Hz).
Plots along image row are also shown.

Interestingly, a simple normalization of the temperature can remove most of the unwanted effects of shape variation (and uneven heating since uniform heating is hardly achieved). The normalization function consists in the division of each frame (k) of the temporal temperature T sequence by the first frame after the heating pulse. This can be expressed by the following equation (Fig. 4 shows some results):

$$T_{k\,normalized} = T_k / T_1 \qquad (8)$$

Following Section 2.2, blind frequencies were then extracted. Since data was subject to noise (as shown on the plots of Fig. 3 and 4), smoothing was performed by fitting the phase data with a logarithmic polynomial (as in temperature reconstruction [9]). Fig. 5 shows the phase for the five different defect depths of the specimen.

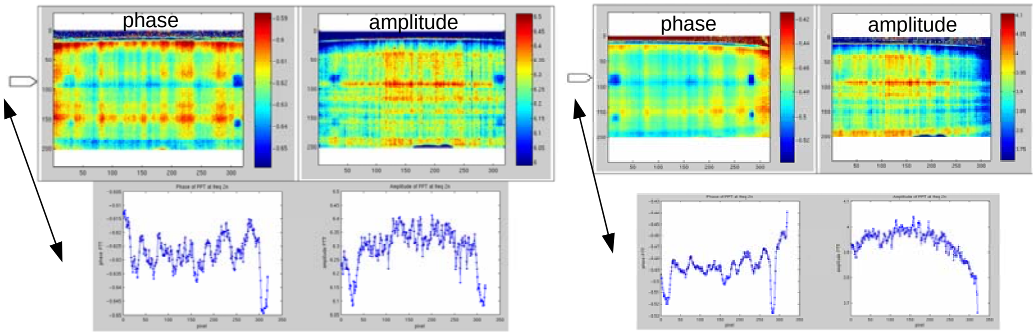

(a) (b)

Fig. 4 Effect of orientation on phase and amplitude for *Specimen* 1 with orientation of (a): 0° and (b): 20°. Second discrete frequency (0.167 Hz). Plots along image row are also shown. Phase and amplitude after normalization of temperature sequence.

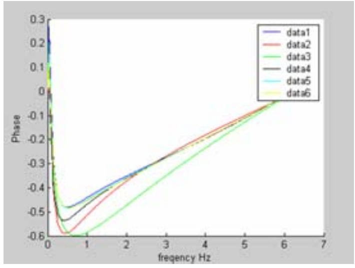

Fig. 5 Typical phase evolution from the shallowest to the deepest defect ranking (0.2 mm increment): 3, 2, 4, 5, 1 and data 6 is the selected reference area (non-defect). Results were obtained using 400 frames at an acquisition speed of 25 Hz, allowing a minimum frequency of 0.0625 Hz and maximum frequency of 12.5 Hz. Specimen orientation was 0°. *Specimen* 1.

Several tests were performed over defects of different sizes yielding to similar blind frequencies. In fact, provided the defect was large enough (size-on-depth ratio >> 1), size does not affect blind frequency (at least as long as the defect can be detected!). In the present study, size-on-depth ratio varies from 3 (minimum) to 75 (maximum). Table 2 summarizes the results for different depths with orientation 0°.

Table 2. Experimental average blind frequencies for different depths (here we refer to depths by specimen plies), *Specimen* 1.

| Orientation: 0° | 5th and 6th ply | 4th and 5th ply | 3rd and 4th ply | 2nd and 3rd ply | 1st and 2nd ply |
|---|---|---|---|---|---|
| blind frequency | 0.75 | 1.2125 | 1.5 | 2.5875 | 7 |

The next step was to study the effect of orientation on blind frequency. Results are presented in Table 3.

Table 3. Experimental average blind frequencies for different depths and orientations. *Specimen* 1.

| Orientation | 5th and 6th ply | 4th and 5th ply | 3rd and 4th ply | 2nd and 3rd ply | 1st and 2nd ply |
|---|---|---|---|---|---|
| 0° | 0.689 | 0.75 | 1.13 | 2.38 | 6.81 |
| 10° | 0.44 | 1.13 | 1.50 | 2.25 | 6.63 |
| 20° | 0.44 | 2.19* | 1.69 | 2.56 | 7.31 |
| 30° | 0.63 | 1.13 | 1.57 | 2.44 | 6.94 |
| 40° | 0.8125 | - | 1.8125 | 2.3750 | 8.00* |
| 40° position 2 | 0.75 | - | 1.25 | 2.25 | 7.06 |
| 50° | 1.06 | - | 1.75 | 2.38 | 7.13 |

* suspected data!

From Table 3, we notice the orientation does not affect significatively the blind frequency, at least if the orientation is reasonable ($\theta < 30°$, Table 1). In fact, if values of Table 3 are averaged (Table 4), we obtained similar values as listed in Table 2.

Table 4. Blind frequency for different depths (averaged values of Table 3). *Specimen* 1.

| | 5th and 6th ply | 4th and 5th ply | 3rd and 4th ply | 2nd and 3rd ply | 1st and 2nd ply |
|---|---|---|---|---|---|
| Mean | 0.69 | 1.30 | 1.53 | 2.38 | 7.13* |
| std | 0.2195 | 0.6195 | 0.2573 | 0.1083 | 0.4449* |

* Removing the value of 8.00 at 40°, a mean of 6.98 and standard deviation of 0.2426 are obtained.

On Fig. 6 the evolution of blind frequency as function of depth is plotted after data of Table 4, such a curve can be used for calibration purpose (eq. 7).

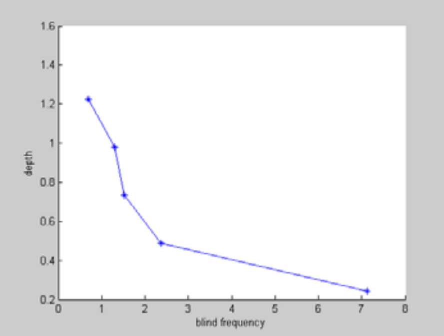

Fig. 6 Blind frequency for different depths. *Specimen* 1.

*Specimen* 2 (GFRP) was similarly tested without application of any paint. Since this material is partly transparent (in both visible and infrared spectra), mitigate results were obtained and a threshold had to be applied to the phase contrast (difference of phase between point of interest and reference area) due to the high noise level. The high noise level prevents the full analysis of defects at all depths. Nevertheless, results from the shallowest defect indicate orientation does not affect the blind frequency, at least for reasonable orientations ($\theta < 30°$, Table 1). Table 5 list the experimental frequencies as function of depth for the 0° orientation case.

Table 5 Averaged blind frequency for different depths with 0° orientation. *Specimen* 2.

| Orientation: 0° | 5th and 6th ply | 4th and 5th ply | 3rd and 4th ply | 2nd and 3rd ply | 1st and 2nd ply |
|---|---|---|---|---|---|
| Mean | 0.39 | 0.97 | 1.83 | 2.46 | 5.57 |

## 4. Conclusion

In this paper, a study of the blind frequency as function of surface orientation was performed. We conclude that, for reasonable orientations ($\theta < 30°$), blind frequencies are not affected by orientation. Moreover, we noted blind frequencies are also size invariant provided that defect size-on-depth ratio is sufficiently high (>> 1). Results were obtained on both CFRP and GRFP. It is recommended to apply a coating on GFRP due to the semi-transparent nature of this material.

## 5. Acknowledgements

The support of Ministère des affaires étrangères du Québec and from Ministri Affari Esteri of Italy is acknowledged.

## 6. References

[1] Maldague X.P.V., Theory *and Practice of Infrared Technology for Non Destructive Testing*, John-Wiley & Sons, 684 p., 2001.
[2] X. Maldague, E. Barker, A. Nouah, E. Boisvert, B. Dufort, L. Fortin, “On methods for shape correction and reconstruction in thermographic NDT,” *II$^{nd}$ Workshop on Advances in signal processing for NDE of Materials*, Kluwer Academic Pub., **E – 262:** 209-224, 1994.
[3] J.F.Pelletier, E. Grinzato, R. Dessì, X. Maldague: “Shape and uneven heating correction for NDT on cylinders by thermal methods”, QIRT 96: 263-268, 1996..
[4] V.P.Vavilov, S.Marinetti: “Pulsed Phase Thermography and Fourier-Analysis Thermal Tomography”, *Russian Journal of Nondestructive Testing*, **35:** 2, pp. 134-145, (from *Defectoscopyia* No.2, pp. 58-71, Russia), 1999.
[5] X. Maldague, S. Marinetti, “Pulse Phase Infrared Thermography,” *J. Appl. Phys*, **79**(5): 2694-2698, 1996.
[6] C. Ibarra-Castanedo, N. P. Avdelidis, X. Maldague “Quantitative Pulsed Phase Thermography Applied to Steel Plates,” *Thermosense XXVII*, **5782**: 342-352, 2005.

[7] Bai W., Won B. S. "Evaluation Defects in Composite Plates under Convective Environments using Lock-In Thermography," Meas. Sci. Technol.s **12**: 142-150, 2001.
[8] Busse G. "Optoacoustic Phase Angle Measurement for Probing a Metal," Appl. Phys. Lett., **36**(10): 815-816, 1979.
[9] Shepard S. M. "Advances in Pulsed Thermography," *Thermosense XXIII*, **4360**: 511-515, 2001.